The Astrophysical Journal, 784:26 (18pp), 2014 March 20 doi:10.1088/0004-637X/784/1/26

FUNDAMENTAL MASS–SPIN–MORPHOLOGY RELATION OF SPIRAL GALAXIES

D. Obreschkow[1,2] and K. Glazebrook[2,3]
[1] International Centre for Radio Astronomy Research (ICRAR), M468, University of Western Australia, 35 Stirling Hwy, Crawley, WA 6009, Australia
[2] ARC Centre of Excellence for All-sky Astrophysics (CAASTRO)
[3] Centre for Astrophysics and Supercomputing, Swinburne University of Technology, P.O. Box 218, Hawthorn, VIC 3122, Australia
Received 2013 December 16; accepted 2014 January 17; published 2014 February 28

ABSTRACT

This work presents high-precision measurements of the specific baryon angular momentum j_b contained in stars, atomic gas, and molecular gas, out to $\gtrsim$10 scale radii, in 16 nearby spiral galaxies of the THINGS sample. The accuracy of these measurements improves on existing studies by an order of magnitude, leading to the discovery of a strong correlation between the baryon mass M_b, j_b, and the bulge mass fraction β, fitted by $\beta = -(0.34 \pm 0.03)\lg(j_b M_b^{-1}/[10^{-7}\,\mathrm{kpc\,km\,s^{-1}}\,M_\odot^{-1}]) - (0.04 \pm 0.01)$ on the full sample range of $0 \leqslant \beta \lesssim 0.3$ and $10^9\,M_\odot < M_b < 10^{11}\,M_\odot$. The corresponding relation for the stellar quantities M_* and j_* is identical within the uncertainties. These M–j–β relations likely originate from the proportionality between jM^{-1} and the surface density of the disk that dictates its stability against (pseudo-)bulge formation. Using a cold dark matter model, we can approximately explain classical scaling relations, such as the fundamental plane of spiral galaxies, the Tully–Fisher relation, and the mass–size relation, in terms of the M–j($-\beta$) relation. These results advocate the use of mass and angular momentum as the most fundamental quantities of spiral galaxies.

Key words: galaxies: bulges – galaxies: fundamental parameters – galaxies: kinematics and dynamics – galaxies: spiral – galaxies: structure – radio lines: ISM

Online-only material: color figures

1. INTRODUCTION

In galaxies, total mass M and orbital angular momentum J are fundamental concepts: they are conserved in isolated systems (invariance), defined in any galaxy (universality), and key to other properties (causality). In fact, M and J collectively dictate the density normalization and radius of the galaxy-system (Mo et al. 1998). They thus set the disk pressure and associated physics, including phase transitions (Blitz & Rosolowsky 2006) and instabilities, that affect observables, such as luminosity and morphology. The key question to be answered here is how the primary morphological feature of disk galaxies, their bulge, depends on M and J.

The fundamental nature of M and J motivates their use as primary parameters to describe galaxies (Hernandez & Cervantes-Sodi 2006). In doing so, it is common to remove the implicit mass scaling of J by adopting the specific angular momentum $j \equiv J/M$. M and j are then independent in terms of basic units (mass versus length^2/time). In this work, M and j are indexed to distinguish between stars ($*$), neutral atomic gas (H I), molecular gas (H_2), and all baryons in the galaxy (b). H I and H_2 include 36% helium in addition to hydrogen, and the term "baryons" refers to the sum of stars, H I, and H_2 without including hot halo gas. The quantities M and j without subindices generally refer to either stars (M_* and j_*) or baryons (M_b and j_b).

The first empirical investigation of galaxies in the M–j space was presented by Fall (1983). He used stellar masses M_* derived from total luminosities and approximate j_* to study two samples: 44 spiral (Sb-Sc) galaxies and 44 elliptical galaxies. In both samples, M_* and j_* were found to follow a relation $j_* = qM_*^\alpha$ with similar exponents $\alpha \approx 2/3$, but a prefactor q about five times lower in elliptical galaxies, indicating a significant loss of angular momentum in their formation history. The exponent $\alpha = 2/3$ is a prediction of the cold dark matter (CDM) theory within some simplistic assumptions, while the factor q depends more subtly on the baryon physics in ways sketched out by Romanowsky & Fall (2012). They revisit the M_*–j_* relation of Fall (1983) using a broader morphology range of 67 spiral (Sa–Sm) and 40 elliptical (E7–S0) galaxies. Their study represents the largest and most comprehensive investigation of galaxies in the M_*–j_* plane to date. One of the prime results is that the Hubble sequence of galaxy morphologies is essentially a sequence of increasing angular momentum at any fixed mass—confirming and refining an original suggestion by Sandage et al. (1970).

A shortcoming in current measurements of angular momentum is that they do not include the contribution of gas and that stellar angular momenta J_* are not actually measured by integrating dJ_* over the spatially and kinematically resolved galaxies. Instead, j_* is approximated as $j_* = kv'r'$, where k is a scalar parameter, v' is a measure of the rotation velocity, and r' a specific type of radius (e.g., Equations (2) and (7) in Romanowsky & Fall 2012). Requiring less data than a full measurement, this approximation can be applied to larger galaxy samples at the cost of introducing random and systematic errors in j_*. More accurate measurements of j_* are technically difficult, because they require deep long-slit spectroscopy or kinematic maps with kiloparsec resolution obtainable via integral field spectroscopy (IFS), which is a quickly rising 21st century technology (Glazebrook 2013). For instance, SAGES Legacy Unifying Globulars and GalaxieS (Arnold et al. 2013), a deep survey on the Keck/DEIMOS spectrograph, revealed converged measurements of j_* in six early-type galaxies (Romanowsky & Fall 2012). Examples of IFS surveys enabling somewhat less accurate (since less deep) measurements of j_* include the ATLAS^{3D} multi-wavelength IFS survey (Cappellari et al. 2011), the Calar Alto Legacy Integral Field Area Survey (Sánchez et al. 2012), the Mapping Nearby Galaxies at APO survey, the survey with the Sydney Australian Astronomical Observatory Multi-Object

Integral Field Spectrograph (Croom et al. 2012), and its proposed highly multiplexed successor (HECTOR, Lawrence et al. 2012).

On the theoretical side, both analytical models and numerical simulations are used to investigate the growth of j. Models assuming that the value of j set by tidal torques during the protogalactic formation of structure (Peebles 1969; Doroshkevich 1970; White 1984) remains conserved during the formation of galaxies, except when large spheroids form, can reproduce the slope and zero-point of the M–j relation (Fall 1983; Romanowsky & Fall 2012). However, until recently, hydrodynamic simulations indicated that j is in fact not conserved, but significantly reduced by dynamical friction during the contraction of the gas. Consequently, simulated galaxies were systematically smaller and bulgier than observed ones (Navarro & Steinmetz 2000; Stinson et al. 2010). This "angular momentum crisis" hindered theoretical inferences from observed angular momenta. It now seems understood that the numerical loss of angular momentum was an artifact associated with insufficient spatial resolution and a lack of supernovae feedback that removes low-j material from the galaxy centers (Governato et al. 2010; Agertz et al. 2011; Guedes et al. 2011; Marinacci et al. 2013). Simulations overcoming these challenges are about to reveal details of the joint growth of mass and angular momentum in galactic disks (e.g., Brooks et al. 2011). In parallel, semi-analytic models of millions of galaxies increasingly focus on angular momentum (Benson 2012) and have already uncovered the importance of the co-evolution of M and j in explaining the cosmic history of star formation (Obreschkow & Rawlings 2009a, 2009b).

With IFS surveys flourishing and accurate simulations of angular momentum in large galaxy samples within reach, angular momentum is becoming a standard tool in galaxy evolution research. This paper explores this new era with the aim to measure the M–j relation in spiral galaxies and its dependence on morphology. Unprecedented precision is achieved using deep high-resolution (<kpc) kinematic data available for 16 spiral galaxies of The H I Nearby Galaxy Survey (THINGS; Walter et al. 2008). The observational accuracy of the resulting j values exceeds existing studies by an order of magnitude, and for the first time the measurements also comprise the contributions of H I and H_2 in addition to stars. Using these data, the M–j–morphology relation of spiral galaxies turns out to be much tighter than previously known (Romanowsky & Fall 2012).

Section 2 introduces the sample of spiral galaxies and the method to compute their angular momenta. Section 3 analyzes the M–j relation (for stars and all baryons) and its dependence on the bulge mass fraction β (often called B/T). A strong three-dimensional (3D) correlation is discovered and discussed in Sections 4 and 5. Section 6 concludes the paper with a summary of the key results. An in-depth analysis of angular momentum contained in different gas phases, as well as additional scaling relations, will be discussed in a sequel paper.

2. MEASUREMENT OF ANGULAR MOMENTUM

2.1. Sample of Spiral Galaxies

This study uses all 16 spiral[4] galaxies of THINGS (Walter et al. 2008), for which stellar and cold gas surface densities have been published by Leroy et al. (2008). This sample, shown in Figure 2 (left) and Table 1, offers the highest quality data to date for a detailed measurement of $j_* \equiv J_*/M_*$, $j_{\rm HI} \equiv J_{\rm HI}/M_{\rm HI}$, and $j_{\rm H_2} \equiv J_{\rm H_2}/M_{\rm H_2}$ in spiral galaxies. The sample covers stellar masses from $10^9\,M_\odot$ to $8\times10^{10}\,M_\odot$ and Hubble types T from Sab to Scd. Figure 1 shows the 16 galaxies in the ($M_{\rm b}$, T)-plane on top of the distribution of galaxies in the H I Parkes All Sky Survey (HIPASS; Barnes et al. 2001) with resolved morphologies and K-band based stellar masses (494 galaxies, see Meyer et al. 2008). This figure reveals that the 16 galaxies nicely represent the majority of spiral galaxies detected in a typical 21 cm/optically limited survey.

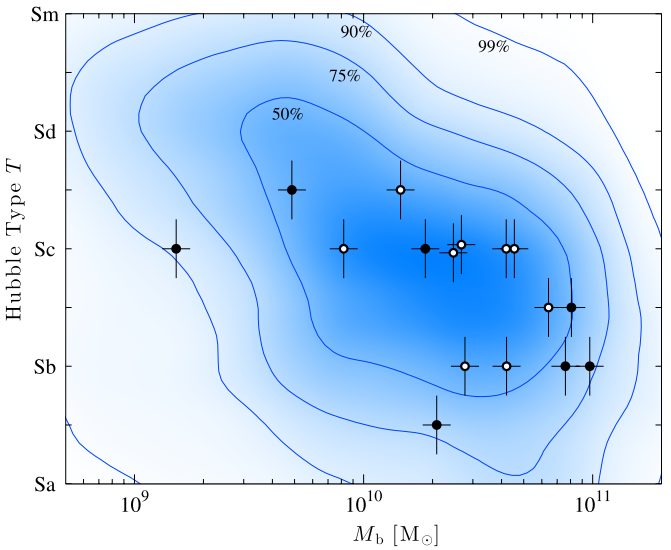

Figure 1. Representation of the 16 barred (open circles) and unbarred (filled circles) spiral galaxies in the ($M_{\rm b}$, T) plane. Error bars are standard deviations of measurement uncertainties. The sample is compared against the 30 times larger reference sample of HIPASS galaxies with measured morphologies and baryon masses (Meyer et al. 2008). The distribution of this reference sample in the ($M_{\rm b}$, T) plane, smoothed by a 2D-Gaussian Kernel matching the (x, y) measurement uncertainties, is shown as a blue density field with contours containing the indicated fraction of galaxies.

(A color version of this figure is available in the online journal.)

2.2. Primary Data

The data collected by Leroy et al. (2008) comprises multi-wavelength maps from different surveys: kinematic H I maps at a mean resolution of 11″ (∼400 pc) and 5 km s^{-1} from THINGS (Walter et al. 2008), far-ultraviolet (FUV) maps of 5.″6 resolution from the space-based *Galaxy Evolution Explorer* (*GALEX*) Nearby Galaxies Survey (Gil de Paz et al. 2007), 24 μm and 3.6 μm infrared (IR) data with a resolution of $\leqslant$6″ from the space-based Spitzer Infrared Nearby Galaxies Survey (SINGS; Kennicutt et al. 2003), CO(1 → 0) maps of 7″ resolution from the Berkeley-Illinois-Maryland Association (BIMA) Survey of Nearby Galaxies (BIMA SONG; Helfer et al. 2003), and CO(2 → 1) maps of 11″ resolution from the HERA CO Line Extragalactic Survey (HERACLES; Leroy et al. 2009).

From these data (Leroy et al. 2008, see Appendices A–E therein) computed radial surface density profiles $\Sigma(r)$ as a function of radius r at a resolution of ∼400 kpc, degrading the raw resolution where necessary. Atomic gas densities $\Sigma_{\rm HI}$ were computed from the integrated intensity maps of the 21 cm emission line. Molecular gas densities $\Sigma_{\rm H_2}$ were estimated from the CO(2 → 1) maps, except in the case of NGC 3627 and NGC 5194, where CO(1 → 0) maps were used instead.

[4] NGC 3077 is listed as an Sd spiral galaxy in Leroy et al. (2008), but upon visual inspection this galaxy is removed, being an irregular object, in agreement with the interaction study of Walter et al. (2002) and the "I0 pec" classification in the NASA/IPAC Extragalactic Database (NED).

Table 1
Properties of the 16 Spiral Galaxies Studied in This Paper

NGC	Type	β	R_* (kpc)	$R_{\rm flat}$ (kpc)	V (km s^{-1})	$M_{\rm b}$	M_*	$M_{\rm gas}$ lg ($M_\odot$)	$M_{\rm H\,I}$	$M_{\rm H_2}$	$j_{\rm b}$	j_*	$j_{\rm gas}$ lg (kpc km s^{-1})	$j_{\rm H\,I}$	$j_{\rm H_2}$
628	Sc	0.04	2.3	0.8	217	10.27	10.1	9.8	9.7	9.0	3.07	2.98	3.23	3.28	2.98
925	SBcd	0.05	4.1	6.5	136	10.16	9.9	9.8	9.8	8.4	3.01	2.94	3.09	3.10	2.95
2403	SBc	0.02	1.6	1.7	134	9.91	9.7	9.5	9.5	7.3	2.85	2.62	3.04	3.08	2.61
2841	Sb	0.10	4.0	0.6	302	10.88	10.8	10.1	10.1	8.5	3.53	3.40	3.91	3.94	3.40
2976	Sc	0.00	0.9	1.2	92	9.18	9.1	8.4	8.3	7.8	2.05	2.03	2.11	2.21	1.93
3184	SBc	0.02	2.4	2.8	210	10.41	10.3	9.7	9.6	9.2	3.09	3.03	3.25	3.32	2.97
3198	SBc	0.03	3.2	2.8	150	10.41	10.1	10.1	10.1	8.8	3.24	2.97	3.45	3.49	3.02
3351	SBb	0.14	2.2	0.7	196	10.44	10.4	9.4	9.2	9.0	2.94	2.91	3.10	3.27	2.75
3521	SBbc	0.16	2.9	1.4	227	10.81	10.7	10.1	10.0	9.6	3.14	3.06	3.38	3.46	2.98
3627	SBb	0.22	2.8	1.2	192	10.62	10.6	9.4	9.0	9.1	2.84	2.84	2.82	2.93	2.77
4736	Sab	0.32	1.1	0.2	156	10.32	10.3	9.0	8.7	8.6	2.37	2.34	2.63	2.86	2.36
5055	Sbc	0.17	3.2	0.7	192	10.91	10.8	10.2	10.1	9.7	3.30	3.18	3.59	3.69	3.08
5194	SBc	0.09	2.8	0.8	219	10.66	10.6	9.8	9.5	9.4	3.19	3.18	3.25	3.12	3.36
6946	SBc	0.10	2.5	1.4	186	10.62	10.5	10.0	9.8	9.6	3.06	3.02	3.17	3.32	2.91
7331	SAb	0.16	3.3	1.3	244	10.99	10.9	10.2	10.1	9.7	3.38	3.35	3.52	3.59	3.30
7793	Scd	0.01	1.3	1.5	115	9.69	9.5	9.2	9.1	(8.6)	2.49	2.43	2.61	2.66	2.40

Notes. The specific angular momenta j were calculated as described in Section 2.3. The bulge mass fractions β were computed as explained in Section 2.2 and illustrated in Figure 14. All other values have been copied from Table 4 in Leroy et al. (2008), inferring $M_{\rm H_2}$ of NGC 7793 from its SFR as described in Section 2.2 and using $M_{\rm gas} = M_{\rm H\,I} + M_{\rm H_2}$ and $M_{\rm b} = M_* + M_{\rm gas}$. As explained by Leroy et al., the scale radius R_* and the rotation parameters $R_{\rm flat}$ and V represent fits to the stellar surface density $\Sigma_*(r) \propto \exp(-r/R_*)$ and H I velocity profile $v(r) = V[1 - \exp(-r/R_{\rm flat})]$. Measurement uncertainties are not shown in this table, but they are plotted as error bars in the figures of Sections 1–5 and accounted for in all results.

These estimates rely on a constant CO-to-H_2 conversion factor $X_{\rm CO(1\to0)} = 2 \times 10^{20}\,{\rm cm^{-2}\,(K\,km\,s^{-1})^{-1}}$ with an additional correction of 1.36 to include helium, and a fixed line ratio $I_{\rm CO(2\to1)} = 0.8 I_{\rm CO(1\to0)}$. Stellar mass densities Σ_* were inferred from the 3.6 μm continuum maps. These maps were first reduced to median radial profiles to minimize the contribution of hot dust and polycyclic aromatic hydrocarbon emission near star-forming regions. The median 3.6 μm profiles were then converted to $\Sigma_*(r)$ by adopting an empirical K-to-3.6 μm calibration and a constant K-band mass-to-light ratio of $\Upsilon_*^K = 0.5\,M_\odot/L_{\odot,K}$, neglecting local variations of a factor ~two between young and old stellar populations. Star formation rate (SFR) surface densities $\Sigma_{\rm SFR}$, used to complete missing H_2 data (see below), were derived from a combination of FUV and far-IR (FIR) 24 μm continuum maps to capture directly visible and dust-obscured star formation (Appendix D of Leroy et al. 2008).

This paper uses the surface density profiles published by Leroy et al. (2008) up to the following variations. First, surface densities $\Sigma_{\rm H\,I}(r)$ were re-derived from the H I intensity maps (Walter et al. 2008), because the $\Sigma_{\rm H\,I}(r)$ published by Leroy et al. are restricted to $\geqslant 1\,M_\odot\,{\rm pc^{-2}}$. From the H I maps most $\Sigma_{\rm H\,I}(r)$ can be measured down to about $10^{-2}\,M_\odot\,{\rm pc^{-2}}$. Using these extended data, it turns out that limiting $\Sigma_{\rm H\,I}$ to $\geqslant 1\,M_\odot\,{\rm pc^{-2}}$ decreases $J_{\rm H\,I}$ and $j_{\rm H\,I}$ by about 20% and 10%, respectively. These percentages improve to 1% and 0.1% if densities down to $10^{-1}\,M_\odot\,{\rm pc^{-2}}$ are included, thus motivating the use of the full data. Second, where CO-based H_2 surface densities are missing, they are estimated using an inverted star-formation law $\Sigma_{\rm H_2} = t_{\rm H_2}\Sigma_{\rm SFR}$, where $t_{\rm H_2} = 1.9 \times 10^9$ yr is the effective H_2 depletion time found by Leroy et al. (2008). This method is used to infer the total H_2 mass of NGC 7793, the full functions $\Sigma_{\rm H_2}(r)$ of NGC 628/925/2403/2841/7793, as well as large-r parts of $\Sigma_{\rm H_2}(r)$ in the other galaxies. Third, the densities $\Sigma_*(r)$ and $\Sigma_{\rm H_2}(r)$ are extrapolated beyond the maximal radii $R_{\rm max}$, to which they were measured or estimated. The extrapolations use an exponential profile $\Sigma_0 \exp(-r/R)$, with parameters Σ_0 and R fitted to the data on the range $r \in [R_{\rm max}/2, R_{\rm max}]$. The extrapolated parts are shown as dashed lines in Figure 16 (left). We emphasize that completing H_2 data from SFRs and extrapolating r beyond $R_{\rm max}$ has no effect on the conclusions of this paper. This post-processing only affects $j_{\rm H_2}$, j_*, and $j_{\rm b}$ by ~10% allowing these values to converge to the 1% level (see Section 2.3).

To study correlations between angular momentum and galaxy morphology, the latter is quantified using the stellar mass fraction β in the bulge. In this paper, "bulge" generically refers to any central stellar over-density without further specifying the nature of the component. In the present sample, these bulges are mostly flattened pseudo-bulges (Kormendy & Fisher 2008), nine of which include a bar component. For each galaxy, β is calculated by fitting $\Sigma_*(r)$ with a model composed of an exponential function for the disk and a Sérsic profile (Sérsic 1963) for the bulge, as described in Appendix A. The resulting values of β are listed in Table 1. The standard errors inferred from resampling are about 0.02.

2.3. Precision Measurement of Angular Momentum

In the approximation of a flat galaxy with circular orbits, the norm of the angular momentum relative to the center of gravity can be written as

$$J = \left| \int dM\, \mathbf{r} \times \mathbf{v} \right| = 2\pi \int_0^\infty dr\, r^2\, \Sigma(r)\, v(r), \qquad (1)$$

where dM is the mass element, $\mathbf{r}$ is the position vector from the center of gravity, $\mathbf{v}$ is the velocity vector, $v(r)$ is the norm of $\mathbf{v}$ at $r = |\mathbf{r}|$, and $\Sigma(r)$ is the azimuthally averaged mass surface density of the considered baryonic component. The specific angular momentum is

$$j \equiv \frac{J}{M} = \frac{\int_0^\infty dr r^2 \Sigma(r) v(r)}{\int_0^\infty dr r \Sigma(r)}. \qquad (2)$$

Computing J and j from axially averaged density and velocity profiles allows the outskirts (to $r \approx 14 R_*$) with low pixel

signal-to-noise to be reliably included, but the use of axially averaged surface densities $\Sigma(r)$ does not, in fact, assume or require Σ to be axially symmetric.

The integral of Equation (2) is evaluated numerically, while correcting for the inclination of the galaxy as detailed in Appendix B. The integrals are evaluated out to the maximal observed H I radius $R_{\rm HI,max} \approx 14R_*$. The only exception is NGC 5194—the Whirlpool Galaxy—where the upper bound of the integral is restricted to 14 kpc to suppress the contributions of the interacting close companion NGC 5195 and associated stripped material. Equation (2) is applied to the different baryonic surface densities, resulting in distinct values of $j_{\rm X} \equiv J_{\rm X}/M_{\rm X}$ for all the baryons ($j_{\rm b}$), stars (j_*), atomic gas ($j_{\rm H\,I}$), molecular gas ($j_{\rm H_2}$), and atomic and molecular gas together ($j_{\rm gas}$). These values are listed in Table 1.

All measurements of j assume that the baryonic material orbits at the circular velocity $v(r)$ of the H I gas. This assumption of co-rotation between H I, H_2, and stars is justified in the rotation supported parts of the galaxy, where $v(r)$ is dictated by the local gravitational force. In the dispersion supported stellar bulge, however, the stellar rotational velocity is generally smaller than that of the H I disk. For example, in the Andromeda galaxy (M31), the bulge rotation at $r \approx$ 0–15 kpc (about 50 km s^{-1}, Dorman et al. 2012) is five times smaller than the disk rotation inferred from H I (about 250 km s^{-1}, Unwin 1983). One might thus suspect that the values of j_* presented here overestimate the real values. This effect is nonetheless negligible in late-type galaxies. In fact, even when using H I velocities $v(r)$ for all stars, the stellar angular momentum J_* of the bulge (according to the bulge–disk decomposition of Equation (A1)) only accounts for 0.3% of the total J_* on average. The most extreme bulge contributions are found in NGC 4736 (1.3%), NGC 3627 (0.6%), and NGC 5055 (0.6%). Thus, the contribution of the angular momentum of the stellar bulge to j_* is smaller than the statistical measurement uncertainties of a few percent for j_* (see the following). Bulges nonetheless affect $j_* \equiv J_*/M_*$ through their mass, which takes values up to 0.32 of the total stellar mass M_* in the present sample.

How accurate are the measurements of j? Let us first discuss statistical uncertainties. By repeating the computations of j via Equation (2) with random Gaussian variations of $\Sigma(r)$ matching their r-dependent measurement uncertainties, it turns out that such uncertainties affect j by less than 0.1%. These errors are negligible relative to those associated and $v(r)$. In computing $v(r)$ via Equation (B4), the inclination-dependent deprojection factor $C(\varphi, i)$ introduces an uncertainty in the normalization of $v(r)$ of 2%–4% for the given inclination uncertainties. A second order uncertainty can result from non-circular orbits, as a non-circular velocity component $v_\perp$, perpendicular to the circular orbit, can perturb the measurement of the circular component $v(r)$. To estimate the magnitude of this effect, we generated 10^5 mock galaxies, inclined at 51° (the average inclination of the present sample), with constant $v(r) = V_0 = 200$ km s^{-1}, and a non-circular dipole component of amplitude $v_\perp = 10$ km s^{-1}, typical for spiral galaxies (e.g., Beauvais & Bothun 1999). For every mock galaxy, the orientation of the non-circular component in the plane perpendicular to the circular motion was chosen randomly. For each mock galaxy, we then recovered a circular velocity V from the line-of-sight component v_z (see Figure 15), assuming only circular orbits. The resulting values V are centered on V_0, but scattered with a standard deviation of 4 km s^{-1} (2%). Hence, the statistical error introduced when assuming circular orbits in the presence of a realistic non-circular component is approximately 2%. Another source of statistical uncertainty is associated with the finite maximal observing radii $R_{\rm max}$. In fact, due to the r^2 term in the angular momentum integral, non-detected, low-density material in the outer ($r > R_{\rm max}$) regions contributes more significantly to J than to M. Thus the question, to what extent j converges within $r \leqslant R_{\rm max}$, requires careful examination. Figure 2 (right) shows the cumulative specific angular momenta $j(r) \equiv \int_0^r dr'\, r^2\Sigma(r')v(r') / \int_0^r dr'\, r\Sigma(r')$ of stars (for H I and H_2 see Figure 16, right). To assess how well these functions have converged, a model for their extrapolation beyond $R_{\rm max}$ is needed. Upon assuming an exponential disk $\Sigma(r) \propto \exp(-r/R)$ rotating at a constant circular velocity V, $j(r)$ becomes

$$j(r) = \left[2 + \frac{(r/R)^2}{1 + r/R - \exp(r/R)}\right] R\, V. \qquad (3)$$

Explicit fits of Equation (3) to the measured $j(r)$ predict that the measured j have converged at the 1% level for $j_{\rm b}$, j_*, and $j_{\rm H_2}$, and at the 10% level for $j_{\rm H\,I}$ and $j_{\rm gas}$. Details and exceptions are given in Appendix B.

The measurements of j might also be subject to systematic errors. Errors in light-to-mass conversions (i.e., luminosity-to-stellar mass and CO-to-H_2) equally affect J and M, thus canceling out in j. Only variations of these conversions within a galaxy can affect j. This might be significant for the CO-to-H_2 conversion, which can vary along r due to a metallicity gradient. A few available measurements for NGC 5194 (Arimoto et al. 1996) suggest that the H_2/CO ratio increases by a factor ∼two on two exponential scale radii. Accounting for this variation increases $j_{\rm H_2}, j_{\rm gas}$, and $j_{\rm b}$ in NGC 5194 by about 20%, 10%, and 2%, respectively. Similar changes might apply to other galaxies in the sample. However, because the CO-to-H_2 conversion remains uncertain (Obreschkow & Rawlings 2009c), this paper maintains the constant value of Leroy et al. (2008). Other errors can result from a breakdown of the flat disk model in the case of disturbed or warped galaxies, but in the present sample such effects are negligible based on visual inspection. Distance errors affect j linearly. The 16 galaxies considered here have Hubble flow distances (Table 1 in Walter et al. 2008) on the order of 10 Mpc with expected uncertainties around 5% that are partially correlated.

In summary, the specific angular momenta have statistical uncertainties of a few percent (3%–5%) for $j_{\rm b}$, j_*, and $j_{\rm H_2}$, and ∼10% for $j_{\rm H\,I}$ and $j_{\rm gas}$. Potential systematic uncertainties are estimated to about 10%.

2.4. Comparison Against Approximate Measurements

Most measurements of angular momentum in the literature do not have detailed kinematic maps at their disposal. They therefore resort to approximations of j based on global measurements. In this section, we compare typical approximations of j_*, labeled as $\tilde{j}_*$, against our precision measurements j_*. Since the typical deviations between $\tilde{j}_*$ and j_* turned out to be much larger than the few percent statistical uncertainties of j_*, the latter can be considered as exact in this comparison.

The most common approximation of j_*, already used by Fall (1983), relies on the flat, exponential disk model of Equation (3). In the limit of $r \to \infty$ this equation reduces to (e.g., Equation (7) in Mo et al. 1998),

$$\tilde{j}_* = 2R_*V, \qquad (4)$$

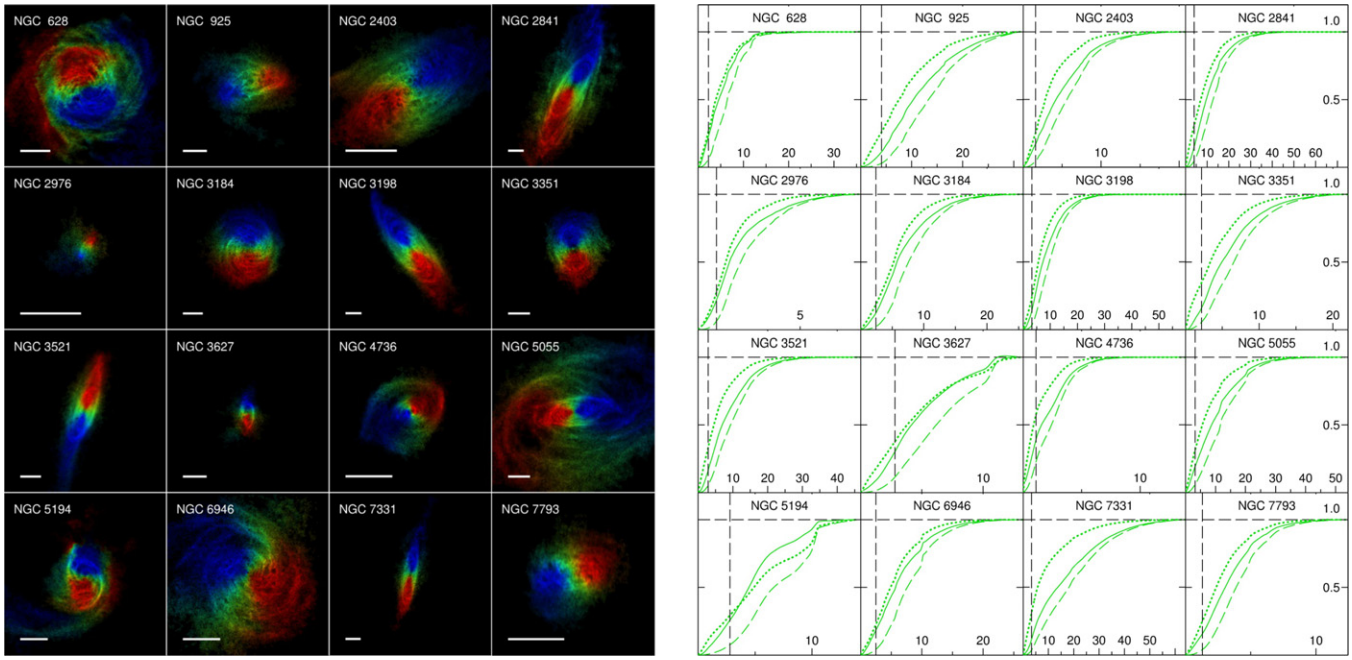

Figure 2. Left: combined H I intensity map and color-coded H I velocity map of the 16 spiral galaxies considered in this work. Colors range from red to blue for projected velocities from $-V \sin i$ to $V \sin i$, where V (Table 1, from Leroy et al. 2008) is the asymptotic rotational velocity and i is the galaxy inclination (Leroy et al. 2008). The white bars represent 10 kpc scales. Right: fraction of the stellar mass M_* (dotted), stellar angular momentum J_* (dashed), and specific stellar angular momentum $j_* = J_*/M_*$ (solid), enclosed within a given radius. The vertical dashed lines represent the exponential scale length R_* (Table 1, from Leroy et al. 2008).

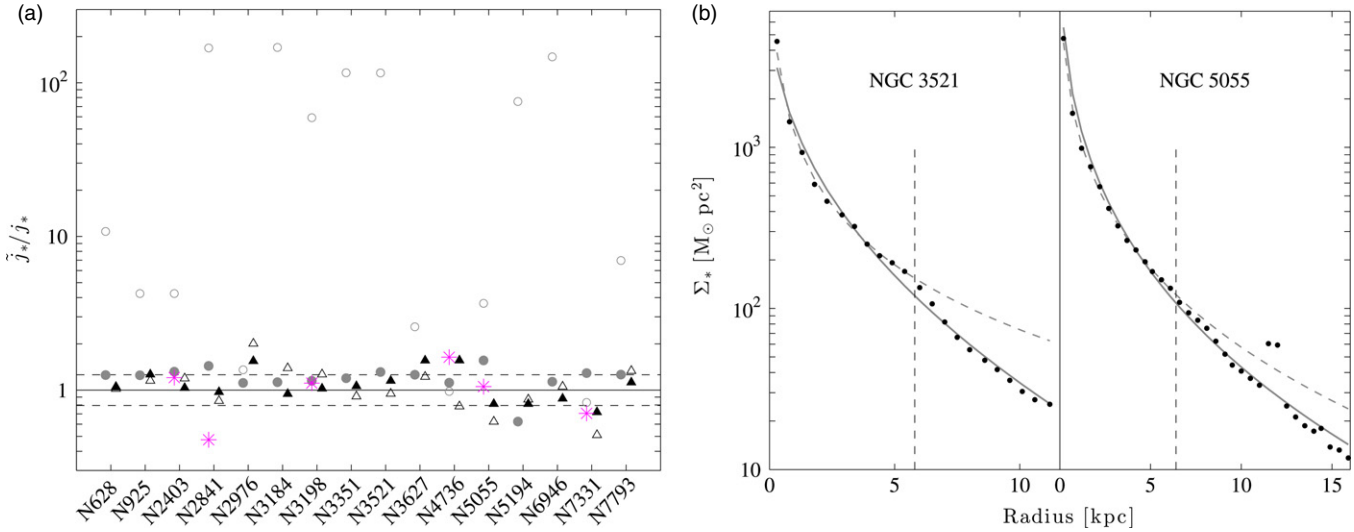

Figure 3. Assessment of approximate methods to measure the specific stellar angular momentum j_*. (a) Approximate values $\tilde{j}_*$, normalized by the full measurements j_*. Triangles represent the exponential disk model of Equation (4), fitted to the full profiles $\Sigma(r)$ (filled triangles) and only to $r \leqslant 2R_*$ (open triangles). Circles represent the Sérsic approximation of Equation (5), fitted to the full profiles $\Sigma(r)$ (filled circles) and only to $r \leqslant 2R_*$ (open circles). Pink stars represent the estimates of j_* from Romanowsky & Fall for the six galaxies also contained in the present sample. (b) Functions $\Sigma_*(r)$ for two selected galaxies. Black dots denote the measurements (Leroy et al. 2008), while lines show the Sérsic fits to the whole data (solid lines) and to $r \leqslant 2R_*$ (dashed lines). Those two types of fits correspond to the filled and open circles in panel (a), respectively. Vertical dashed lines denote the limit $r = 2R_*$.

requiring only the exponential scale radius R_* of the stellar disk and the (constant) circular velocity V. Those two parameters can be estimated from other measurements, for instance $R_* \approx 0.6r_e \approx 0.3r_{25}$, where r_e is the "effective radius" containing half the light and r_{25} is the "isophotal radius" with a B-band surface brightness of 25 mag arcsec^{-2}. The velocity V can be estimated from the total H I linewidth or from optical linewithds at the radius r_{25} (or beyond), corrected for turbulence and galaxy inclination. Figure 3(a) (triangles) shows the values $\tilde{j}_*$ given by Equation (4), normalized to the reference values j_*. Filled triangles use R_* and V derived from the full stellar surface densities $\Sigma_*(r)$ and deprojected velocity profiles $v(r)$; they are the values R_* and V (Table 1) adopted from Leroy et al. (2008). Open triangles use approximate scale radii, fitted only to $r \leqslant 2R_*$. In general, this approximation based on the exponential disk model provides remarkably good results. The rms error of $\tilde{j}_*$ for all 16 galaxies is about 30% (0.10 dex). Using only data within $r \leqslant 2R_*$, this rms error increases to 40% (0.14 dex).

Another approximation, introduced by Romanowsky & Fall (2012), builds on the flat disk model with a surface

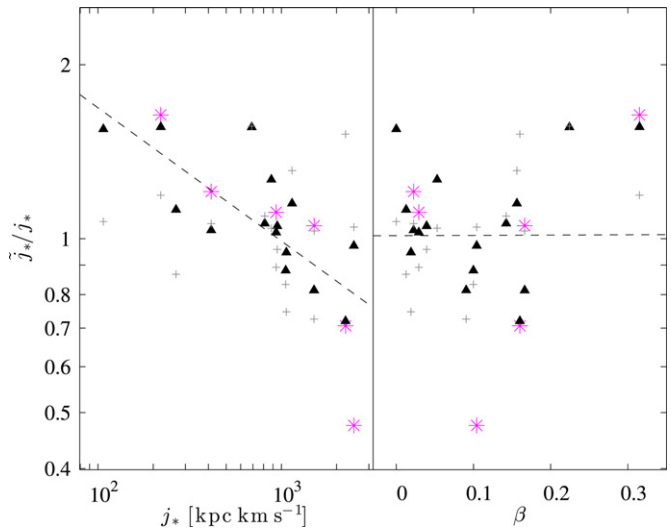

Figure 4. Approximate specific angular momenta $\tilde{j}_*$, calculated with Equation (4) (triangles) and adopted from Romanowsky & Fall (2012; pink stars), deviate systematically from j_*. This dependence is fitted by Equation (6), shown as dashed line in the left panel. This relation can be explained by a systematic variation of the stellar surface density and rotation curve with galaxy mass. Accounting for these variations removes the correlation between j_* and $\tilde{j}_*/j_*$ (crosses). No significant correlation is detected between $\tilde{j}_*/j_*$ and β.

(A color version of this figure is available in the online journal.)

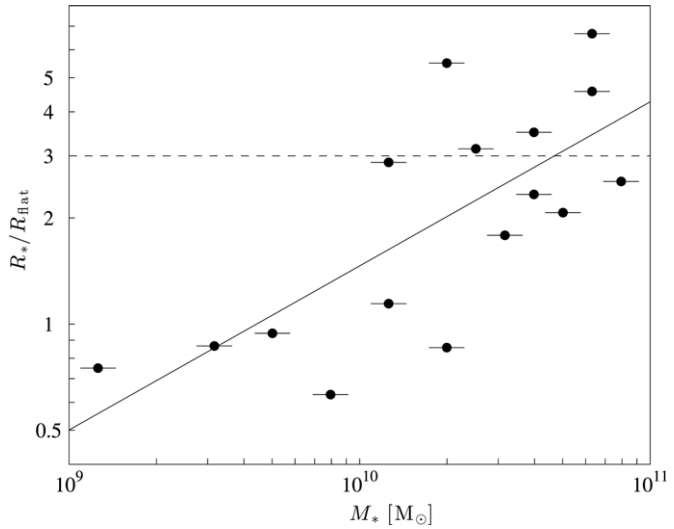

Figure 5. Dependence of the disk concentration, parameterized by $R_*/R_{\rm flat}$, on stellar mass M_* (values from Leroy et al. 2008, shown in Table 1 of this paper). The solid line represents a standard linear regression, whereas the dashed line indicates the value $R_*/R_{\rm flat} = 3$, typical for Milky Way-sized spiral galaxies.

density described by the Sérsic profile $\Sigma(r) \propto \exp[-b_n(r/r_{\rm e})^{1/n}]$ with free parameters $r_{\rm e}$ and n ($n = 1$ for exponential disk, $n = 4$ for a de Vaucouleurs profile). The factor $b_n \approx 2n - 1/3 + 0.009876/n$ ensures that r_e is the effective radius, $\int_0^{r_{\rm e}} dr\, r\, \Sigma(r) = 0.5 \int_0^{\infty} dr\, r\, \Sigma(r)$. Romanowsky & Fall find that j_* is approximated by

$$\tilde{j}_* = k_n v_{\rm s} r_{\rm e}, \tag{5}$$

where v_s is the deprojected rotation velocity measured at a radius $2r_{\rm e}$ and $k_n \approx 1.15 + 0.029n + 0.062n^2$. To test this approximation the 16 galaxies of this work were fitted with single Sérsic functions, once using the whole profiles $\Sigma_*(r)$, once artificially restricting them to radii $r \leqslant 2R_*$, where R_* is again the exponential scale radius given by Leroy et al. (2008). The velocities $v_{\rm s} = v(2r_{\rm e})$ are then taken as the average of the de-projected H I velocity $v(r)$ between $1.9r_{\rm e}$ and $2.1r_{\rm e}$. The resulting approximations $\tilde{j}_*$ are shown in Figure 3(a) (circles). If the Sérsic functions are fitted to the full data (filled circles in Figure 3(a)), that is roughly within $r \leqslant 14R_*$, the rms error is about 30% (0.11 dex), comparable to the exponential disk model. However, when fitting only within $r \leqslant 2R_*$ (open circles), the rms error heavily increases to 2500% (1.4 dex), with $\tilde{j}_*$ being systematically larger than j_*. This large error can be traced back to the fact that Sérsic functions fitted to the inner ($r \leqslant 2R_*$), bulgier part of the galaxy, systematically overestimate the surface density at larger radii by overestimating the index n, as illustrated in Figure 3(b). In conclusion, the Sérsic approximation of Equation (5) is much more prone to errors than the exponential disk approximation of Equation (4).

Romanowsky & Fall (2012) do not, in fact, use the Sérsic approximation of Equation (5) to estimate j_* of spiral galaxies because they also find the Sérsic fits to be too uncertain. Instead, they adopt a more robust approach that separates the galaxy into an exponential disk and a smaller "classical" bulge with a de Vaucouleurs profile (fixed Sérsic index $n = 4$). For both components j_* is approximated separately and then recombined. Six of the Romanowsky galaxies are also in the present sample. Their values $\tilde{j}_*$, plotted in Figure 3 (pink stars), yield an rms error of about 50% (0.17 dex).

A serious concern is that the errors of the approximations $\tilde{j}_*$ correlate significantly with j_* (albeit not with β), as shown in Figure 4. This correlation applies both to the $\tilde{j}_*$ calculated via Equation (4) (triangles in Figure 4) and to those determined by Romanowsky & Fall (2012; pink stars). The correlation is best fitted by the dashed line in Figure 4(a), which can be rewritten as

$$\left[\frac{j_*}{10^3\ {\rm kpc\ km\,s^{-1}}}\right] \approx 1.01 \left[\frac{\tilde{j}_*}{10^3\ {\rm kpc\ km\,s^{-1}}}\right]^{1.3}. \tag{6}$$

This non-linearity between j_* and $\tilde{j}_*$ is traceable to two features. Firstly, the stellar surface density $\Sigma_*(r)$ systematically deviates from an exponential in such a way that the fraction f_J of stellar angular momentum outside the half-light radius $r_{\rm e}$ increases with mass. This fraction ranges from about $f_J \approx 75\%$ at $M_* = 10^9 M_\odot$ to $f_J \approx 85\%$ at $M_* = 10^{11} M_\odot$. To account for the high values of f_J and their variability, the scale radius R_* used in Equation (4) can be fitted on $r > r_{\rm e}$ rather than on the whole disk. When doing so, the correlation between $\lg(\tilde{j}_*/j_*)$ and $\lg(j_*)$ is reduced by 60%. The remaining 40% are traceable to a systematic variation of the rotation curves $v(r)$ with mass. This can be seen by looking at the fits (Boissier et al. 2003)

$$v(r) \approx V\left[1 - \exp\left(-\frac{r}{R_{\rm flat}}\right)\right] \tag{7}$$

performed by Leroy et al. (2008); their best-fitting parameters V and $R_{\rm flat}$ are listed in Table 1. The ratio between Leroy's stellar scale radius R_* and $R_{\rm flat}$ is found to increase with M_*, roughly by a factor of three per dex in M_*, as shown in Figure 5 (see also de Blok et al. 2008). Thus, the normalized rotation curves $v(r/R_*)/V$ increase faster in more massive galaxies—an effect that is also seen in radial variations of the Tully–Fisher (TF) relation in larger galaxy samples (Yegorova & Salucci 2007). We can account for this effect by convolving Equation (7)

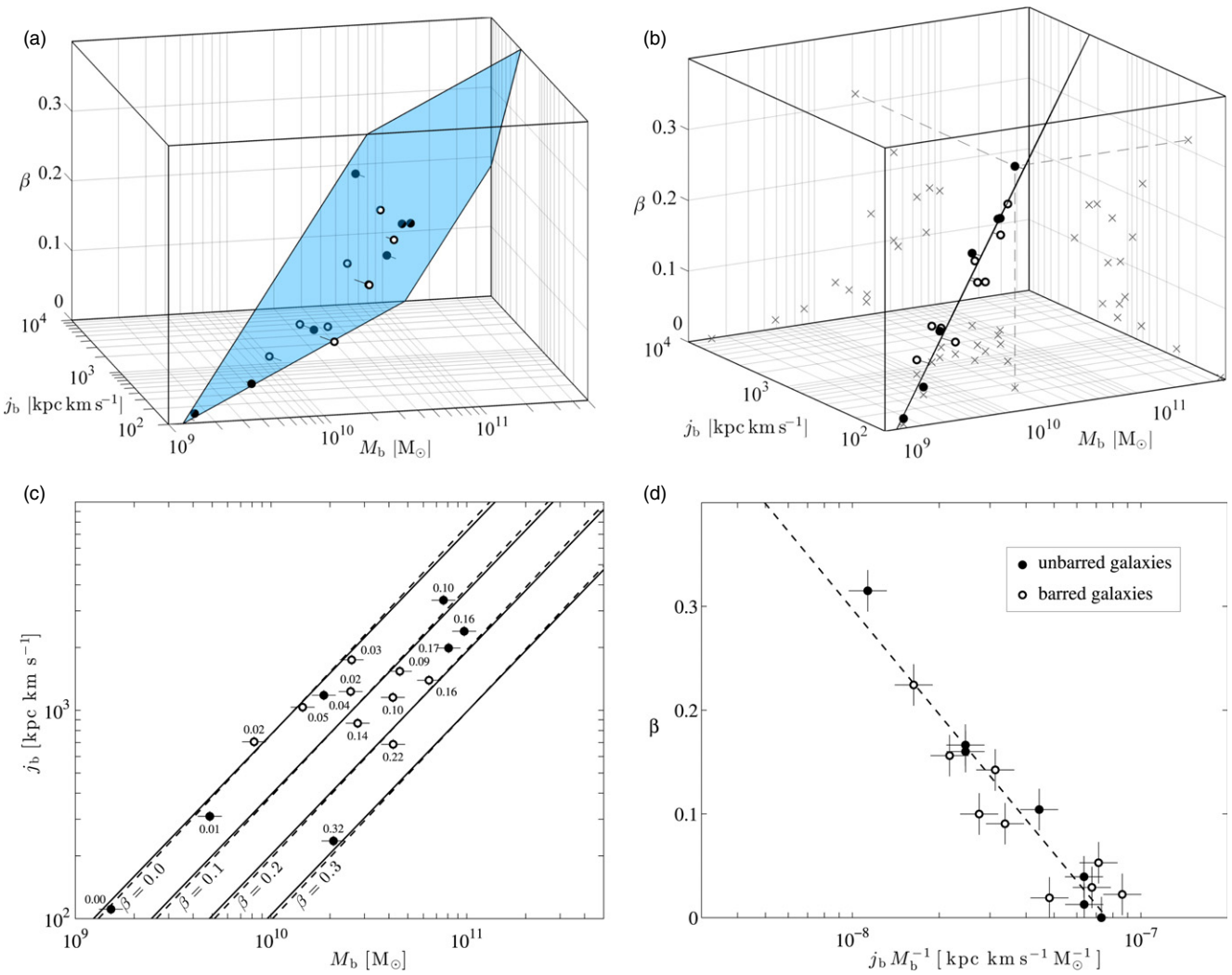

Figure 6. Four panels show different projections of the 16 spiral galaxies in (M_b, j_b, β) space. Unbarred and barred galaxies are represented by filled and open circles, respectively. The projections of the 16 data points onto the three planes (M_b, j_b), (M_b, β), and (j_b, β) are represented by the crosses in panel (b). The blue plane in panel (a) is the best trivariate fit to the data (in log-log-lin space), as given in Equation (9). The same plane is shown edge-on as a solid line in panel (b) and at discrete values of β as solid lines in panel (c). The dashed lines, representing Equation (11), are the best fit to the data when imposing a linear dependence between β and $\lg(j_b/M_b)$, which implies $j_b \propto M_b$ at any fixed β. This fit becomes a single dashed line in panel (d) and one dashed line of slope 1 for every value β in panel (c). The small numbers next to the data points in panel (c) show their β values. Error bars represent standard deviations of the measurement uncertainties. For clarity, these error bars are only displayed in panels (c) and (d).

(A color version of this figure is available in the online journal.)

with an exponential surface density $\Sigma_*(r) \propto \exp(-r/R_*)$ in Equation (2). This solves to

$$\tilde{j}_* = 2R_* V \frac{(R_* + R_{\rm flat})^3 - R_{\rm flat}^3}{(R_* + R_{\rm flat})^3}. \quad (8)$$

Using Equation (8) with R_* fitted to $\Sigma_*(r)$ on $r > r_e$ completely removes the correlation between j_* and $\tilde{j}_*/j_*$ (crosses in Figure 4(a)). In conclusion, $\tilde{j}_*$ approximated by Equation (4) and Romanowsky & Fall (2012) is offset from j_* via Equation (6) due to a systematic mass dependence of the disk shape and rotation curve.

3. PHENOMENOLOGY OF THE M–j–β RELATION

This section explores the 3D relationship between M, j, and the bulge mass fraction β of the 16 late-type ($0 \leqslant \beta \lesssim 0.3$) galaxies from the THINGS sample considered in this work. Throughout this section, M and j refer to the baryonic M_b and j_b or the stellar M_* and j_*.

3.1. Fundamental Empirical Relationships

Intriguingly, the 16 spiral galaxies turn out to be highly correlated in (M, j, β) space. Figure 6 shows this space in four alternative projections, revealing that the data form a plane in the space spanned by $\lg M_b$, $\lg j_b$, and β, where "lg" denotes the base 10 logarithm. Importantly, this M–j–β relation does not seem to be affected by central bars—a feature worth investigating in future studies.[5] The plane can be expressed as

$$\beta = k_1 \lg\left[\frac{M}{10^{10}\,M_\odot}\right] + k_2 \lg\left[\frac{j}{10^3\ {\rm kpc\ km\,s^{-1}}}\right] + k_3, \quad (9)$$

where k_1, k_2, and k_3 are free parameters, fitted to the data using a trivariate regression (Appendix C) that accounts for normal measurement errors in all three dimensions. The best fits are

[5] Using 10,674 disk galaxies from SDSS, Cervantes-Sodi et al. (2013) found evidence for a dependence of bars on the galactic spin parameter, with unbarred galaxies occupying an intermediate range of spin parameters between short- and long-barred ones.

$(k_1, k_2, k_3) = (0.34 \pm 0.03, -0.35 \pm 0.04, -0.04 \pm 0.02)$ if $(M, j) = (M_\mathrm{b}, j_\mathrm{b})$, and $(k_1, k_2, k_3) = (0.31 \pm 0.03, -0.33 \pm 0.05, -0.02 \pm 0.02)$ if $(M, j) = (M_*, j_*)$. The intervals denote 68% confidence intervals of the correlated uncertainties. Equation (9) is represented by the plane in Figures 6(a) and (b). The correlation between the measured values of β and those predicted by Equation (9) is surprisingly high, with a Pearson correlation coefficient of 0.95. The reduced χ^2 of the fit is 0.9; thus the deviations of the data from the fit are entirely accounted for by measurement errors. In other words, the data is consistent with zero intrinsic scatter off Equation (9). Another interesting feature is that Equation (9) is irreducible in the sense that it cannot be explained based on the two-dimensional (2D) relations M–j, M–β, and j–β. This is best seen when projecting the data onto the three planes (crosses in Figure 6(b)). In any of these planes, the reduced χ^2 (14.4, 11.5, and 18.1) of a linear regression is significantly higher than in 3D.

When discussing the data in the (M, j)-plane it is convenient to rewrite Equation (9) as

$$\frac{j}{10^3\,\mathrm{kpc\ km\,s^{-1}}} = k\xi(\beta)\left[\frac{M}{10^{10}\,M_\odot}\right]^\alpha, \qquad (10)$$

where $\xi(\beta) = \exp[-g\beta]$ (obtained when exponentiating Equation (9)) is a bulge-dependent scaling factor equal to unity in the case of a pure disk ($\beta = 0$). The best-fitting parameters are $(k, \alpha, g) = (0.77 \pm 0.07, 0.98 \pm 0.06, 6.65 \pm 1.02)$ if $(M, j) = (M_\mathrm{b}, j_\mathrm{b})$, and $(k, \alpha, g) = (0.89 \pm 0.11, 0.94 \pm 0.07, 7.03 \pm 1.35)$ if $(M, j) = (M_*, j_*)$. Equation (10) is shown as solid lines in Figure 6(c) for different values of β. Interestingly, the exponent α is consistent with $\alpha = 1$. Upon imposing $\alpha = 1$, the best fit to Equation (10) is $(k, g) = (0.76 \pm 0.05, 6.83 \pm 0.61)$ for all baryons and $(k, g) = (0.91 \pm 0.09, 7.59 \pm 0.79)$ for stars only. This fit is shown as dashed lines in Figure 6(c). Given $\alpha = 1$, Equation (10) can then be rewritten as

$$\beta = k_1 \lg\left[\frac{jM^{-1}}{10^{-7}\,\mathrm{kpc\ km\,s^{-1}}\,M_\odot^{-1}}\right] + k_2 \qquad (11)$$

with $(k_1, k_2) = (-0.34 \pm 0.03, -0.04 \pm 0.01)$ for baryons and $(k_1, k_2) = (-0.30 \pm 0.03, -0.01 \pm 0.01)$ for stars. Equation (11) is shown as dashed lines in Figure 6(d).

3.2. Stars versus Baryons

The M–j–β relation turns out to be surprisingly similar for all baryons (star+cold gas) and for stars alone (Figure 7). In fact, the fitting parameters for baryons and stars (given below Equation (9)) are consistent within their uncertainties. This is due to the fact that adding cold gas approximately moves the galaxies in the (M, j) plane along lines of constant β (blue lines in Figure 7). In other words, the transition from stars to baryons essentially moves the galaxies inside a fixed M–j–β plane. Formally, the close similarity between the relations M_b–j_b–β and M_*–j_*–β is due to the fact that β varies approximately as $j_\mathrm{b}M_\mathrm{b}^{-1}$ coupled with the fact that $j_\mathrm{b}M_\mathrm{b}^{-1} \approx j_*M_*^{-1}$. The latter equation is possible, as the contribution of cold gas to the baryon angular momentum J_b (about 34% on average) is higher than the contribution of cold gas to M_b (about 23%).

The similarity between the relations M_b–j_b–β and M_*–j_*–β might break down if dwarf galaxies of much higher gas fractions were included. The precise relationship between angular momentum in stars and different cold gas phases will be discussed in a sequel paper.

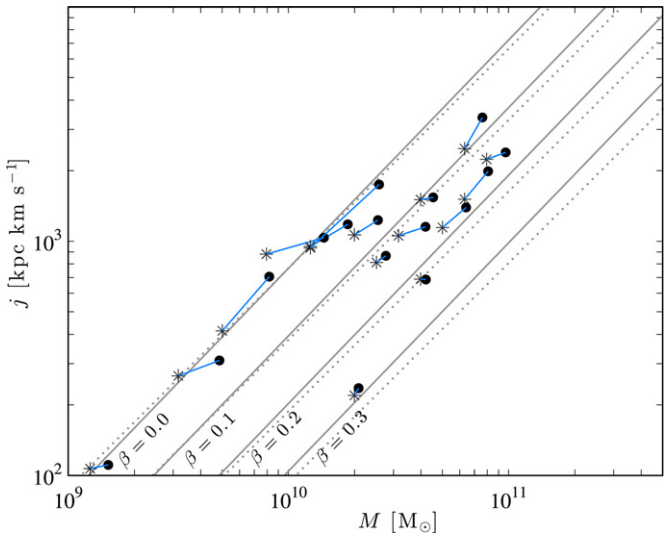

Figure 7. Comparison of the M–j distribution for baryons (filled dots) and stars (stars). Identical galaxies are connected by blue lines. Gray lines are the fits (Equation (10)) at different bulge mass fractions β for baryons (solid lines) and stars (dotted lines).

(A color version of this figure is available in the online journal.)

3.3. Comparison Against Earlier Studies

Having established the M–j–β relation in Section 3.1, we now compare this relation against published data. No significant sample of spiral galaxies with detailed measurements of angular momentum, based on summation of sub-kiloparsec maps, has yet been published. All approximate measurements are restricted to stellar angular momentum without including gas. Thus, this comparison is restricted to samples of approximate stellar angular momentum. The largest and broadest sample was recently published by Romanowsky & Fall (2012), who estimated the stellar angular momenta in a broad mass-range of spiral, lenticular, and elliptical galaxies. Here, we focus on the 67 spiral galaxies listed in Table 4 of Romanowsky & Fall. This table contains bulge mass fractions β, based on the r-band bulge-disk decomposition of Kent (1986, 1987, 1988), stellar masses M_* based on Two Micron All Sky Survey K-band photometry, and approximate stellar angular momenta j_* estimated from global size and velocity measurements (see Section 2.4). Given the irreducible 3D-correlation between M_*, j_*, and β, the average M_*–j_* relation is a poor and potentially misleading estimator for the comparison of two data sets with different β distributions. Therefore, the comparison of the 16 THINGS galaxies against the 67 Romanowsky galaxies must be performed in (M_*, j_*, β)-space or several projections thereof.

The top panels in Figure 8 show two projections of the M_*–j_*–β relation: the M_*–j_* relation and the $(j_*M_*^{-1})$–β relation. These are the same projections as those in the bottom panels of Figure 6 (but for stars instead of all baryons). Clearly, the Romanowsky data deviate significantly and systematically from the THINGS data in all three coordinates. This deviation is dominated by differences in measurement techniques, not by systematic differences between the two samples, as can be seen from the six galaxies that are in both samples, connected by lines in Figure 8. Upon careful inspection, the following features explain the offset of the Romanowsky points.

M_* axis. Since Romanowsky & Fall use a K-band mass-to-light ratio of $1\,M_\odot/L_{\odot,K}$, while THINGS data (Leroy et al. 2008) assumed $0.5\,M_\odot/L_{\odot,K}$, the stellar masses of

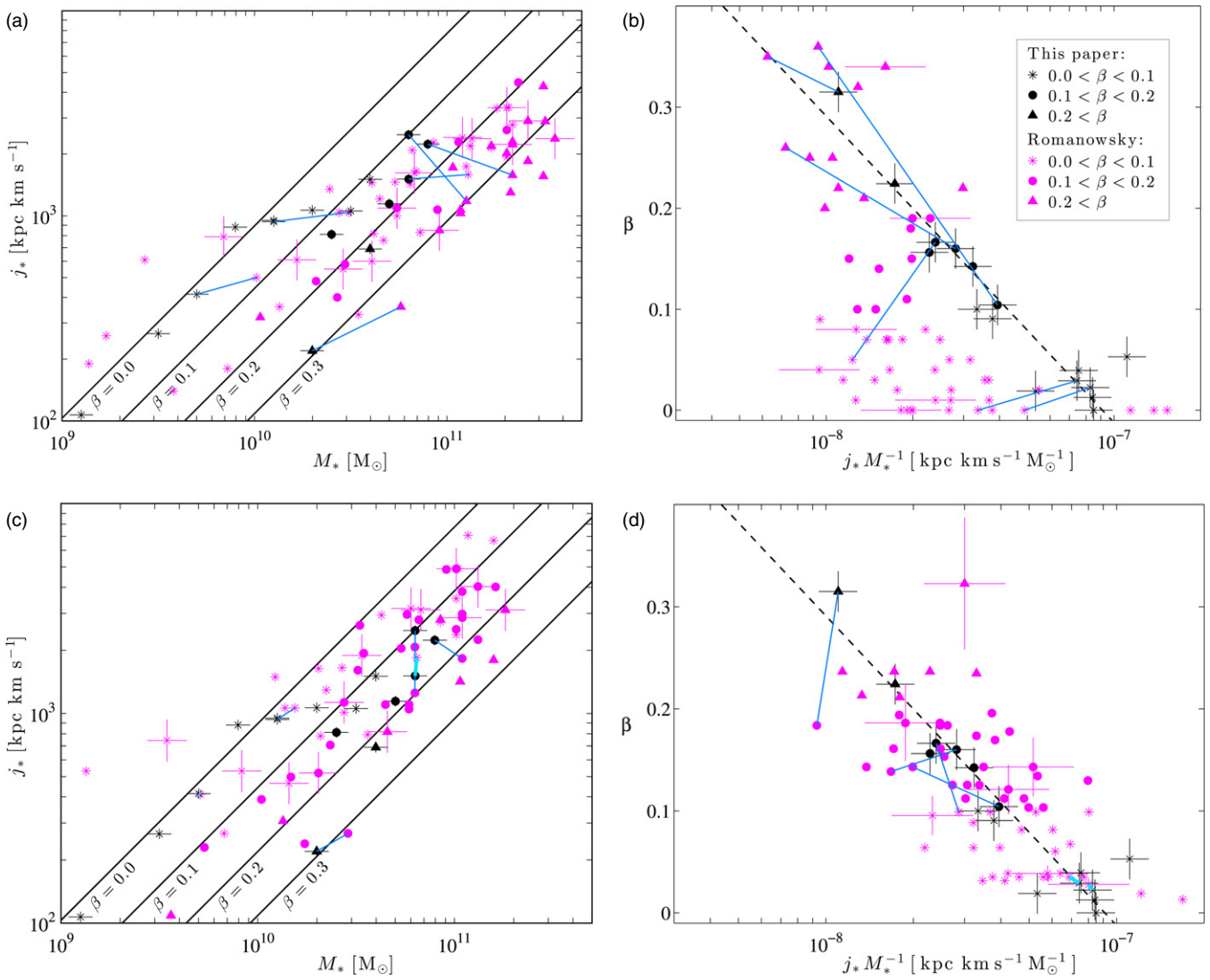

Figure 8. Comparison of the 16 spiral galaxies in the THINGS sample (black) against the 67 spiral galaxies in the sample of Romanowsky & Fall (2012; pink). The six galaxies present in both samples are connected with blue lines. Left and right panels show two different projections of the (M_*,j_*,β) space. Different symbols separate the three ranges of the bulge fraction β. The THINGS points are identical in the top and bottom panels. They represent M_* as given by Leroy et al. (2008) and j_* and β determined in this paper. The Romanowsky points in the top panels are those given in Table 4 of Romanowsky & Fall (2012), while those in the bottom panels have been corrected in all three coordinates to allow a fairer comparison; in particular, the j_* values have been rescaled using Equation (6) and the bulge fractions β have been computed from the Hubble types (details in Section 3.3). The solid lines in panels (a) and (c) represent the fit of Equation (10) for discrete values of β, while the dashed lines in panels (b) and (d) represent the fit of Equation (11). Error bars represent standard deviations of the measurement uncertainties. For clarity, only some error bars are shown. Note that the uncertainties of β in Romanowsky & Fall (2012) are difficult to estimate; therefore no vertical error bars are shown for the Romanowsky data in panel (b).

(A color version of this figure is available in the online journal.)

Romanowsky masses must be rescaled by a factor 0.5 for the purpose of this comparison.

j_* axis. As explained in Section 2.4, the approximate values $\tilde{j}_*$ of Romanowsky systematically differ from the fully measured j_*. This systematic offset can be corrected by rescaling the $\tilde{j}_*$ values using Equation (6).

β axis. The bulge mass fractions of the Romanowsky data, which were adopted from Kent (1986, 1987, 1988), differ significantly from those of the THINGS data, as revealed by the six overlapping objects in Figure 8(b). Their numerical values are as follows.

NGC :	2403	2841	3198	4736	5055	7331
$\beta_{\rm Kent}$ =	0.00	0.36	0.00	0.35	0.05	0.26
$\beta_{\rm THINGS}$ =	0.02	0.10	0.03	0.32	0.17	0.16

Kent decomposed the galaxies by performing 2D fits to *r*-band images. They only assumed that the disk and the bulge have elliptical isophotes in projection, without imposing a disk/bulge model. By contrast, most other studies, including this paper, fit a specific disk and bulge model. The comparison of these two methods is difficult, even more so when applied to different wavebands. However, the Kent decompositions can be verified against the more recent 2D bulge–disk decompositions in *H* band by Weinzirl et al. (2009). They assumed exponential disks and Sérsic bulges, analogous to our decomposition of the THINGS galaxies. Of their 143 galaxies, five overlap with those in the Romanowsky sample.[6] The respective bulge mass

[6] None of the 143 galaxies in the sample of Weinzirl et al. (2009) overlaps with the 16 THINGS galaxies used here.

fractions disagree considerably.

NGC :	1087	2775	4062	4698	7217
$\beta_{\rm Kent} =$	0.00	0.20	0.03	0.55	0.25
$\beta_{\rm Weinzirl} =$	0.00	0.61	0.02	0.22	0.54

Due to this discrepancy, the values $\beta_{\rm Kent}$ adopted in the Romanowsky sample are not appropriate for the purpose of comparison with the present data. We therefore re-estimate the bulge mass fractions of the Romanowsky galaxies from their numerical Hubble types T (drawn from HyperLeda (Paturel et al. 2003) and listed in Table 4 of Romanowsky & Fall 2012). To compute β from T, we use the mean T–β relation of Weinzirl et al. (2009), shown as blue squares in their Figure 14.[7]

The three adjustments of M_*, j_*, and β in the Romanowsky data are justified and necessary for a fair comparison with the present study. Given these adjustments, the data become consistent with the THINGS data (Figure 8, lower panels). In fact, the trivariate fit of Equation (10) to the Romanowsky data with assumed statistical uncertainties of 0.1 dex in M_* and j_* and 20% for β, gives $(k, \alpha, g) = (0.99 \pm 0.15, 0.92 \pm 0.06, 7.63 \pm 0.99)$ in full agreement with the respective parameters of the THINGS galaxies for $(M, j) = (M_*, j_*)$. The reduced χ^2 of this fit is 1.7; thus the scatter of the Romanowsky data is roughly accounted for by observational uncertainties. In this sense the Romanowsky data fully supports the scaling relations of Section 3.1.

4. DISCUSSION OF THE 2D M–j RELATION

In preparation for discussing the full M–j–β relation (Section 5), this section discusses the distribution of the spiral galaxies in the (M, j) plane, relative to predictions from a simplistic analytical model.

4.1. The (M, j) Plane in Basic CDM

In the model of a singular isothermal spherical CDM halo (Mo et al. 1998) of truncation radius $R_{\rm h}$ and dynamical mass $M_{\rm h}$, Newtonian gravity sets the circular velocity to

$$V_{\rm h} = (G M_{\rm h}/R_{\rm h})^{1/2}, \tag{12}$$

where G denotes the gravitational constant. For $V_{\rm h}$ to be constant (isothermicity), the mass density needs to vary as $\rho(r) = V_{\rm h}^2 (4\pi G r^2)^{-1}$ $\forall r \leqslant R_{\rm h}$. Thus the potential energy becomes $E_{\rm pot} = -M_{\rm h} V_{\rm h}^2$. Following the virial theorem ($2E_{\rm kin} = -E_{\rm pot}$), the total energy is

$$E_{\rm h} = -0.5 M_{\rm h} V_{\rm h}^2. \tag{13}$$

Halos are embedded in the cosmic background field of mean density $\rho_c = 3H^2(8\pi G)^{-1}$, where H is the Hubble "constant" at the considered epoche. The halo radius $R_{\rm h}$ can then be defined as the radius to which orbits are approximately virialized. In the spherical collapse model (Cole & Lacey 1996), the mean density enclosed by $R_{\rm h}$ is about $200\rho_c$, thus $\rho(R_{\rm h}) = (200/3)\rho_c$. It follows that

$$R_{\rm h}^3 = 10^{-2} G H^{-2} M_{\rm h}. \tag{14}$$

Equations (12)–(14) are the essential scaling relations of the isothermal CDM halo. This model is manifestly scale-free (at fixed H) in that all global quantities depend on a single scale-factor (e.g., on $R_{\rm h}$) via

$$V_{\rm h} \propto R_{\rm h} \propto M_{\rm h}^{1/3} \propto |E_{\rm h}|^{1/5}. \tag{15}$$

When dealing with the halo angular momentum $J_{\rm h}$, the spin parameter (Steinmetz & Bartelmann 1995)

$$\lambda \equiv J_{\rm h} |E_{\rm h}|^{1/2} G^{-1} M_{\rm h}^{-5/2} \tag{16}$$

has the advantage of being approximately invariant during the growth of a halo in the absence of major mergers (Figure 1 in Stewart et al. 2013). Combining Equation (16) with the scaling equations of the isothermal halo,

$$j_{\rm h} \equiv \frac{J_{\rm h}}{M_{\rm h}} = \sqrt{2}\,\lambda\, R_{\rm h} V_{\rm h} = \frac{\sqrt{2}\,\lambda\, G^{2/3}}{(10H)^{1/3}} M_{\rm h}^{2/3}. \tag{17}$$

If the baryon angular momentum remains conserved during galaxy formation, then the initial equality $j_{\rm b} = j_{\rm h}$ for a uniform mixing of baryons and dark matter applies at all times. More generally, we can define the ratio $f_{\rm j} \equiv j_{\rm b}/j_{\rm h}$, which is unity in the conserved case. Further introducing the baryon mass fraction $f_{\rm M} \equiv M_{\rm b}/M_{\rm h}$,

$$j_{\rm b} = \frac{\sqrt{2}\,\lambda\, f_{\rm j}\, f_{\rm M}^{-2/3}\, G^{2/3}}{(10H)^{1/3}} M_{\rm b}^{2/3}. \tag{18}$$

Adopting the local $H = 70\,{\rm km\,s^{-1}\,Mpc^{-1}}$ and conventional units, Equation (18) becomes

$$\frac{j_{\rm b}}{10^3\,{\rm kpc\ km\,s^{-1}}} = 1.96\,\lambda f_{\rm j} f_{\rm M}^{-2/3} \left[\frac{M_{\rm b}}{10^{10}\,M_\odot}\right]^{2/3}. \tag{19}$$

This equation is equivalent to Equation (15) of Romanowsky & Fall (2012) upon adopting the same H and substituting $f_{\rm M} = f_{\rm b} f_\star$, where $f_{\rm b} = 0.17$ is the universal baryon fraction (Komatsu et al. 2011).

To compare Equation (19) against the THINGS data, the dimensionless parameters need to be given sensible values. The spin parameter λ can be determined from cosmological simulations that tackle the formation of halos, including the tidal build-up of angular momentum. N-body simulations find present-day values around $\lambda \approx 0.04$ with an intrinsic scatter of about 0.02 and no significant correlation to $M_{\rm h}$ (Macciò et al. 2008; Knebe & Power 2008). The baryon fraction $f_{\rm M}$ depends on the galaxy mass and is maximal for intermediate, Milky Way mass galaxies (McGaugh et al. 2010; Behroozi et al. 2013). The mean of the stellar mass considered here being approximately equal to that of the Milky Way, we adopt the constant[8] value of the Milky Way, estimated[9] to $f_{\rm M} \approx 0.05$. Regarding the spin fraction $j_{\rm b}$, high-resolution simulations of four Milky Way-type galaxies (Stewart et al. 2013) find present day values of $f_{\rm j} \approx 1$ within about 50%. Given those choices, $1.96\lambda f_{\rm j} f_{\rm M}^{-2/3}$ can vary between 0.14 and 1.3, spanning the gray-shaded zone of Figure 9.

[7] For fractional values of T, the values of β are interpolated linearly between the neighboring integers of T. For $T \geqslant 7$ (Sd-Sm), the observed trend for $0 \leqslant T < 7$ is extrapolated using the fit $\beta = [(10 - T)/16]^{2.5}$, but this extrapolation has little bearing as it only concerns galaxies with $\beta < 0.015$.

[8] A variable value $f_{\rm M}(M)$, fitted to available data slightly bends the gray-shaded zone of Figure 9 without changing the conclusions.

[9] Based on the empirical values of $M_{\rm h}$ (McMillan 2011), M_* (Flynn et al. 2006), $M_{\rm H\,I}$ (fit to $\Sigma_{\rm H\,I}(r)$ in Kalberla & Dedes 2008), and $M_{\rm H_2}$ (fit to $\Sigma_{\rm H_2}(r)$ in Table 3 of Sanders et al. 1984). Explicit values given in Table 1 of Obreschkow et al. (2011).

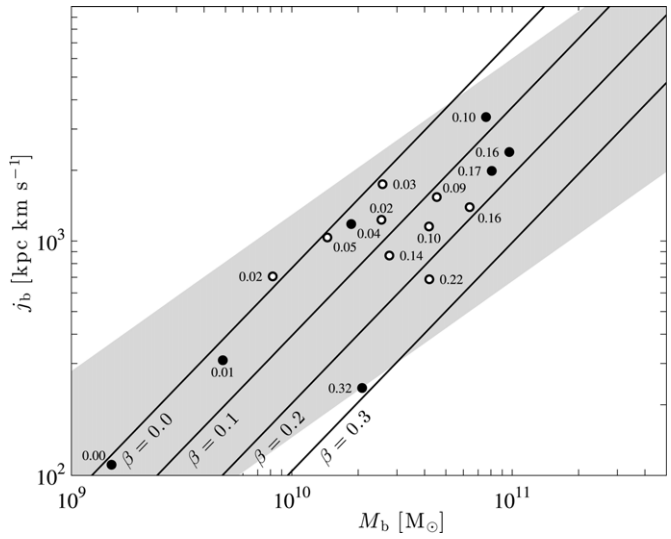

Figure 9. CDM predicts that regular galaxies in isolated halos fall inside the shaded region of the (M_b, j_b) plane, given by Equation (19). This region has an average slope of $\alpha = 2/3$. The data agrees with this prediction, although for a fixed bulge fraction β the power-law index is stepper ($\alpha \approx 1$, solid lines). Points and lines are the same as in Figure 6(c), which shows the errors bars.

In summary, isolated spiral galaxies evolved without major mergers, abnormal feedback, or otherwise exotic histories, are predicted to lie in the shaded zone of Figure 9. This prediction is consistent with the data. Coupling this prediction of a mean relation $j_b \propto M_b^\alpha$, where $\alpha = 2/3$, with the empirical finding of $\alpha \approx 1$ for fixed β's (solid lines in Figure 9), implies that more massive spiral galaxies tend to have higher bulge fractions than less massive ones. This trend qualitatively agrees with observations of the stellar mass function split into Sa, Sb, Sc, and Sd types (Read & Trentham 2005).

4.2. Linking the (M, j) Plane to Classical Scaling Laws

The (M, j) plane is linked to the fundamental plane (FP) for spiral galaxies (Koda et al. 2000; Han et al. 2001; Courteau et al. 2007), a 3D relation between total luminosity L, disk scale radius R, and asymptotic velocity[10] V, forming a plane in log-space. Projected onto 2D (Figure 10), the FP reduces to the L–R relation, the R–V relation, and the V–L relation. The last, known as the TF relation, appears to be a nearly edge-on projection of the FP (Shen et al. 2002).

In the scale-free approximation of Section 4.1, a direct link between the FP and the (M, j) plane appears, because the three quantities L, R, and V scale with M and j (here, $M \approx M_b \approx M_*$, $j \approx j_b \approx j_*$, and $R \approx R_*$). First, the luminosity is a linear proxy of mass, $L \propto M$. Second, in an exponential disk at constant circular velocity, the scale radius becomes $R = j/(2V)$ (Equation (4)). Third, the velocity V can be approximated by the halo velocity $V_h \propto M_h^{1/3}$ (Equation (15)); thus, $V \propto M^{1/3}$ when assuming a constant disk mass fraction M/M_h. Hence the transformation $(M, j) \mapsto (L, R, V)$ writes

$$L \propto M, \quad R \propto jM^{-1/3}, \quad V \propto M^{1/3}. \tag{20}$$

This mapping is sketched schematically in Figure 10. It implies that one can reconstruct the FP of spiral galaxies from their distribution in the (M, j) plane. This distribution is described by $j = kM^{2/3}$ (Equation (18)), where k is a λ-dependent, scattered parameter (gray shading in Figure 9). Combining $j = kM^{2/3}$ with Equations (20), the projected relations of the FP become

$$R \propto kL^{1/3}, \quad V \propto k^{-1}R, \quad L \propto V^3. \tag{21}$$

These scalings are remarkably similar to those found by Courteau et al. (2007) in I band for a sample of 1300 spiral galaxies of all Hubble types (S0a-Sm). Their fits are $R \propto L^{0.32\pm0.02}$ (scatter $\sigma_{\ln R} = 0.33$), $R \propto V^{1.10\pm0.12}$ ($\sigma_{\ln R} = 0.38$), $V \propto L^{0.29\pm0.01}$ ($\sigma_{\ln V} = 0.13$). The scatter of the third scaling—the TF relation—is significantly smaller than that of the other two, relative to the range spanned by the data (Figure 3 in Courteau et al. 2007). This difference in scatter is elegantly explained by the fact that the first two relations in Equations (21) depend on k, while the TF relation does not, as it is an exactly edge-on projection of the FP in our simplistic model.

The three relations of Equation (21) are consistent with the present sample, where $L = L_K$ and $R = R_*$, as shown in Figure 11 (first three panels). Solid lines are power-laws with zero-points fitted to the data and exponents fixed according to Equation (21). Shaded regions denote standard deviations. The location of a galaxy in these planes depends on its position in the (M, j) plane, which systematically depends on β (Section 3); thus the visible offset from between open and filled points in Figure 11. The TF relation exhibits the smallest scatter relative to the range of the data. This had to be expected from the TF being an edge-on projection of the FP in the model discussed so far. In reality, the TF relation is not exactly an edge-on projection of the FP, as explained by the more detailed theory of Shen et al. (2002). Therefore, the offset of galaxies from the mean TF relation correlates with their location in the (M, j) plane, thus with β (hence departing from Equation (21), right). This explains the slight morphology dependence of the TF relation (Kannappan et al. 2002), also visible in the present sample. In fact, we can minimize the scatter of the TF relation by heuristically substituting $\lg L_K$ for $\lg L_K - u\beta$ with $u \approx 2$ (last panel in Figure 11).

In summary, within the model of an exponential disk inside a CDM halo, the FP results from mapping the 2D (M, j) plane into 3D (L, R, V) space via Equations (20). This mapping approximately explains the three classical scaling relations that are the 2D projections of the FP, such as the TF relation. The morphology dependence of these three relations can then be traced back to the M–j–β relation established empirically in Section 3.

5. DISCUSSION OF THE 3D M–j–β RELATION

In the previous section, the β dependence of M–j relation was considered an empirical fact, useful to explain the morphology dependencies of other relations. Any physical explanation of the full M–j–β relation is expected to answer questions such as: What physical processes dominate this relation? Is it self-regulated such that galaxies offset from the relation will evolve back onto it? Which of the quantities M, j, and β are the cause and the effect? These questions call for a model that can reproduce the M–j–β relation from more fundamental scaling laws, time-independent physics (e.g., conservation laws and stability criteria), or time-dependent models (e.g., semi-analytic models or hydrodynamic simulations). In Section 5.1, an explanation based on independent M–j relations for disks and

[10] Sometimes the integrated velocity dispersion is considered rather than V, but in the present context the FP refers to the L–R–V relation.

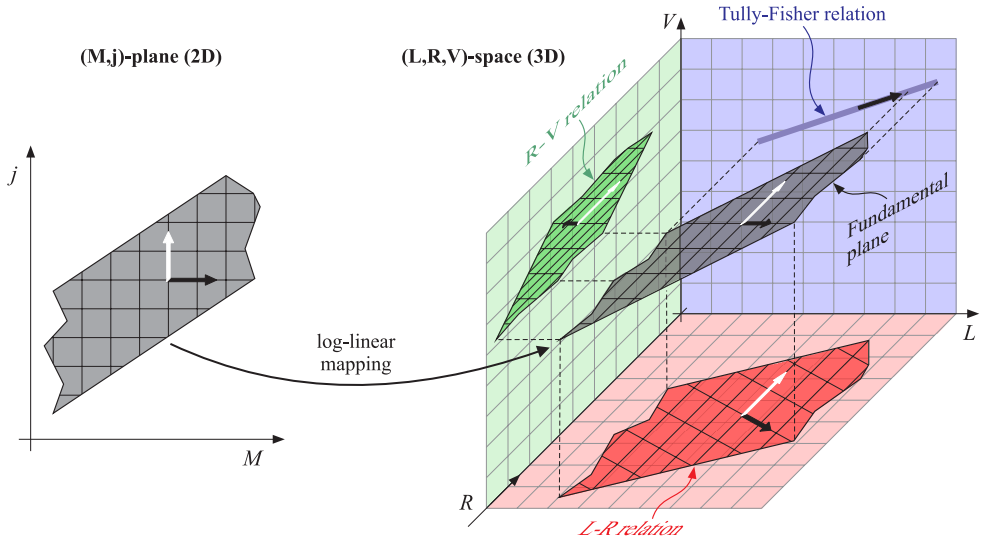

Figure 10. In the model of an exponential disk inside a spherical CDM halo, the FP of spiral galaxies can be understood as a mapping of the (M, j) plane (left) into (L, R, V) space (right) via Equations (20). Projections of the FP onto the (L, R) plane (red), (R, V) plane (green), and (V, L) plane (red), then gives rise to three classical scaling relations, which are given in Equations (21). Of these relations, the V–L relation—the TF relation—has the smallest scatter, because it is a nearly edge-on projection of the FP.

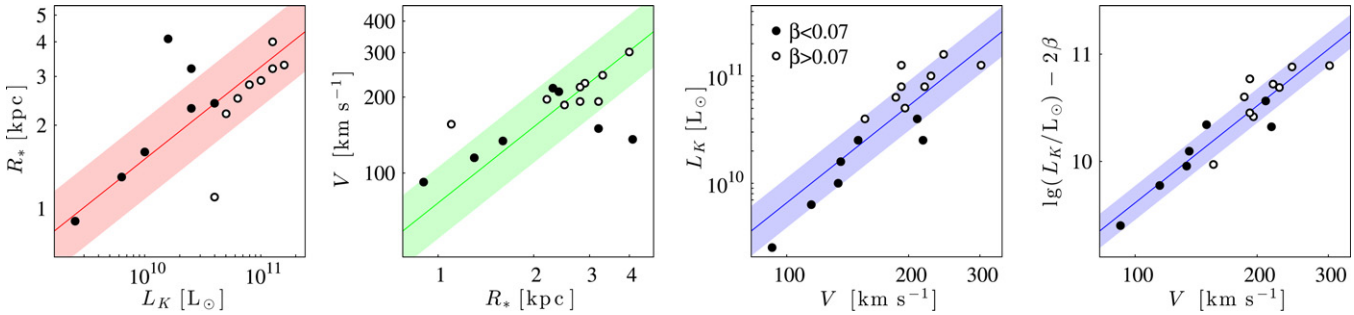

Figure 11. Sixteen spiral THINGS galaxies shown in four different planes. The first three panels depict the orthogonal projections of the FP plane, shown in Figure 10 with matching colors. The fourth panel is identical to the third (the TF relation), except for an additional β term on the vertical scale that factors out the morphology dependence of the TF relation, thus reducing its scatter. Solid lines are power laws with zero-points fitted to the data and fixed exponents of 1/3, 1, 3, and 3, respectively, as predicted by the scale-free model (Equation (21)). Shaded regions represent 1σ scatter.

bulges is shown to be at odds with the data. A path toward an alternative explanation is then discussed in Section 5.2.

5.1. Failure of the Two-component Model

When discussing the Hubble type-dependence of the M–j relation, Fall (1983) and Romanowsky & Fall (2012) invoked the idea that this dependence might result from different, fixed M–j relations for pure disks and pure bulges. While this idea might be valid for classical bulges in bulge-dominated systems, the data of this paper dispels the hope for such an elegant explanation in the case of spiral galaxies with smaller (pseudo-)bulges.

Let us assume—ad absurdum—that disks and bulges do indeed obey independent M–j relations. This assumption can be understood in two ways, formalized via the following models. In "model 1," disk and bulge are strictly independent in the sense that they obey different relations $j_{\rm disk} = kM_{\rm disk}^{\alpha}$ and $j_{\rm bulge} = fkM_{\rm bulge}^{\alpha}$ with constants $k > 0$ and $f > 0$. In "model 2," the angular momenta of disk and bulge both depend on the same total mass $M = M_{\rm disk} + M_{\rm bulge}$ (i.e., $j_{\rm disk} = kM^{\alpha}$ and $j_{\rm bulge} = fkM^{\alpha}$). In both models, the total specific angular momentum $j = (1-\beta)j_{\rm disk} + \beta j_{\rm bulge}$ becomes

$$j = k\xi(\beta)\, M^{\alpha}, \tag{22}$$

where $\xi(\beta) = (1-\beta)^{1+x} + f\beta^{1+x}$ with $x = \alpha$ for model 1 and $x = 0$ for model 2. Intermediate models can then be obtained by choosing $0 < x < \alpha$. Considering this range for x, choosing f between $f = 0$ (zero-rotation bulge model of Mo et al. 1998) and $f = 0.2$ (empirical value of Fall & Romanowsky 2013), and adopting the empirical $\alpha \approx 1$ (Equation (10)), implies that $\xi(\beta)$ falls within the shaded region of Figure 12. By contrast, $\xi(\beta) = \exp[-g\beta]$ determined empirically (see below Equation (10)) varies as the solid line in Figure 12. This measurement is clearly inconsistent with any plausible model of independent disk and bulge relations—an unrealistic $\alpha \approx 6$ or $f < 0$ would be required to match up the model with the data. Therefore, the initial assumption of independent M–j relations for disks and bulges cannot be true.

This conclusion can be confirmed explicitly by measuring the M_*–j_*–β relation of the disk component only. The stellar mass of the disk $M_{\rm disk} = \beta M_*$ is drawn directly from the stellar bulge-disk decompositions (Appendix A). The specific stellar angular momentum of the disk $j_{\rm disk}$ is computed via Equation (2), substituting $\Sigma(r)$ for the disk stellar mass surface density, again drawn from our bulge–disk decompositions. Figure 13 shows the resulting relation projected onto the $(j_{\rm disk}M_{\rm disk}^{-1}, \beta)$ plane. It turns out that $j_{\rm disk}M_{\rm disk}^{-1}$ correlates strongly with β, hence explicitly rejecting the model of a fixed M–j relation for the disk component. Disks with more massive bulges in their centers have lower specific angular momentum, thus smaller radii for a given mass.

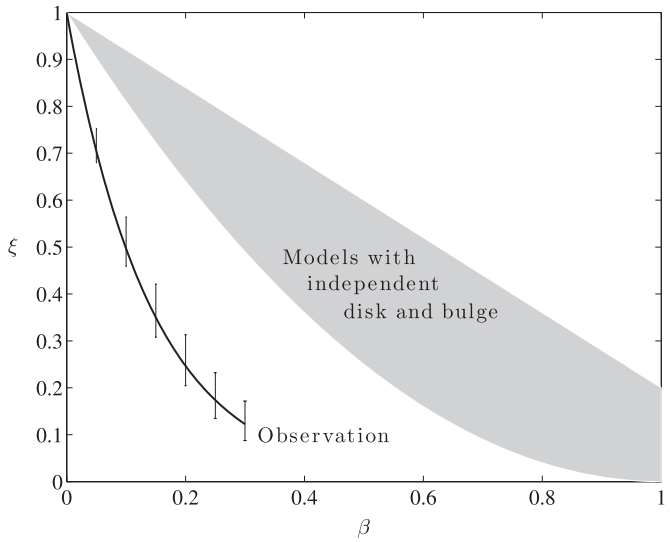

Figure 12. Function $\xi(\beta)$ defined in Equation (22). The solid line represents the measured function for stars (see Equation (10)), whereas the shaded region represents the plausible range if the M–j–β relation were explainable based on independent, fixed M–j relations for pure disks and pure bulges.

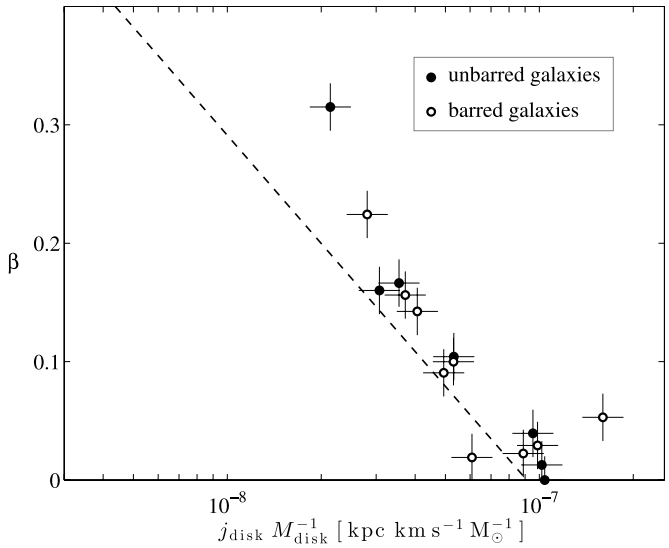

Figure 13. Projection of the M–j–β relation using only the mass and angular momentum of the stellar disk, excluding the bulge. The dashed line shows the best fit to the data for the whole bulge–disk system, this is the same dashed line as in Figure 8(d). This relation is offset to the left, because the small j of the bulge reduces the value of jM^{-1} compared to $j_{\rm disk}M_{\rm disk}^{-1}$.

In summary, disks "know" about the bulges via their angular momentum—an interesting feature that must be accounted for by any model of the M–j–β relation.

5.2. Surface Density Approach to the M–j–β Relation

Late-type galaxies grow their (pseudo-)bulges in situ (Elmegreen et al. 2008; Weinzirl et al. 2009), rather than via major mergers (mass ratios > 0.3) thought to produce the classical bulges of early-type galaxies (Koda et al. 2009). Yet, the β dependence of the $M_{\rm disk}$–$j_{\rm disk}$ relation in late-type systems (Section 5.1) rules out the tempting idea that low-j material simply migrates toward the bulge until the surrounding disk satisfies a certain bulge-independent criterion, such as a universal stability threshold. A more dynamic explanation is needed to account for the β dependence of $j_{\rm disk}$.

To uncover the origin of the M–j–β relation, let us note that this relation is approximately a monotonic relation between β and jM^{-1}, similarly for baryons and stars, as $j_{\rm b}M_{\rm b}^{-1} \approx j_*M_*^{-1}$ according to Section 3.2. Therefore, understanding the M–j–β relation reduces to understanding the quantity jM^{-1} and its effect on bulge formation. As for the first step, it is easily shown that jM^{-1} is a measure of the surface density. In fact, using Equation (4), the surface density scale $\Sigma_0 \propto MR^{-2}$ can be rewritten as $\Sigma_0 \propto Mj^{-1}R^{-1}V$. Assuming a constant velocity $V = V_{\rm h}$ and using $V_{\rm h} \propto HR_{\rm h}$ (from Equations (12) and (14)), gives $\Sigma_0 \propto HMj^{-1}R_{\rm h}R^{-1}$, where $R_{\rm h}$ is the halo radius. If $R \propto R_{\rm h}$ (corresponding to constant λ and $f_{\rm j}$), then

$$\Sigma_0 \propto HMj^{-1}. \tag{23}$$

Thus, jM^{-1} scales inversely with the surface density (or the "concentration") of the galaxy baryons. In this way, our finding that the bulge mass fraction β scales inversely with jM^{-1}, confirms earlier evidence (Prieto et al. 1989) for a relation between the morphology of spiral galaxies and their mean surface density.

Less obvious is the physics behind the connection between the surface density and β. Assuming that the bulge forms from instabilities in the gas-rich protogalaxies, the characteristic bulge growth rate $\dot{M}_{\rm bulge}/M$ and the final bulge mass fraction β are expected to decrease monotonically with the stability of the protogalaxy. Locally, the stability of a flat disk against Jeans instabilities is quantified by the parameter $Q = \sigma\,\kappa\,(3G\Sigma)^{-1}$ (Toomre 1964), where σ is the local velocity dispersion, κ is the orbital frequency, and Σ is the local surface density. By extension, the mean stability of the disk is then characterized by a global parameter $\overline{Q} \propto \sigma_0\kappa_0\,\Sigma_0^{-1}$, where σ_0, κ_0, and Σ_0 are normalization factors of the dispersion, orbital frequency, and surface density, respectively. For circular orbits, $\kappa_0 \propto VR^{-1} \propto HR_{\rm h}\,R^{-1}$. Assuming again that $R \propto R_{\rm h}$, yields $\kappa_0 \propto H$ and

$$\overline{Q} \propto H\sigma_0\Sigma_0^{-1}. \tag{24}$$

Substituting Σ_0 in Equation (24) for Equation (23), the explicit H dependence disappears and

$$\overline{Q} \propto \sigma_0 jM^{-1}. \tag{25}$$

This derivation shows that, up to variations in σ_0, a basic CDM-based galaxy model coupled with an instability-driven bulge can qualitatively account for the monotonic relation between jM^{-1} and β.

The detailed processes governing the in situ formation of bulges as a function of the Q parameter, including the physics of the velocity dispersion σ, remain subject to numerical modeling. Recent high-resolution hydrodynamic simulations with radiative feedback (Elmegreen et al. 2008; Bournaud et al. 2014) suggest that the semi-stable, gas-rich progenitors of modern spiral galaxies partially collapsed into giant star-forming clumps, which survived the strong radiative feedback over timescales required to spiral to the galaxy center by dynamical friction. According to Bournaud et al., this clump-feeding of the bulge can approximately account for the bulge mass of typical spiral galaxies in the local universe and explain the observed structure and outflows of clumps in galaxies at redshift $z \approx 2$ (Genzel et al. 2011). However, the question whether giant clumps survive long enough to migrate to the galaxy center remains debated as summarized by Glazebrook (2013): simulations still allow for both short (Genel et al. 2012)

and long lifetimes (Ceverino et al. 2012), depending on the model assumptions, and the observations remain non-conclusive (Genzel et al. 2011; Wuyts et al. 2012; Guo et al. 2012). Details on clumps aside, the success of high-resolution hydrodynamic simulations with radiative feedback in explaining the structure of spiral galaxies is encouraging and suggests that such simulations might hold the key to explaining the M–j–β relation. However, to date, such simulations still represent a major computational challenge (Section 1).

5.3. Intuitive Summary of the M–j–β Scaling

In essence, the M–j–β scaling can be explained from similarity considerations summarizing Sections 4.1 and 5.2. Assuming self-similarity in 3D, the mass M_h of a halo is proportional to its characteristic volume R_h^3. Newtonian gravity then implies a circular velocity $V_\mathrm{h} \propto (M_\mathrm{h}/R_\mathrm{h})^{1/2} \propto R_\mathrm{h}$. Thus,

$$V_\mathrm{h} \propto R_\mathrm{h} \propto M_\mathrm{h}^{1/3}. \tag{26}$$

Given these relations and a fixed λ, the specific angular momentum is $j_\mathrm{h} = J_\mathrm{h}/M_\mathrm{h} \propto (\lambda R_\mathrm{h} M_\mathrm{h} V_\mathrm{h})/M_\mathrm{h} \propto M_\mathrm{h}^{2/3}$. This scaling extends to M and j in baryons/stars, up to variations in the ratios M/M_h and j/j_h. Thus,

$$j \propto M^{2/3}. \tag{27}$$

The scatter of this relation due numerically predicted variations in λ, M/M_h, and j/j_h, approximately covers the shaded region in Figure 9 for local spiral galaxies.

If the bulge grows from disk instabilities set by the 2D surface density MR^{-2}, then β scales monotonically with $MR^{-2} \propto MR_\mathrm{h}^{-2} \propto Mj^{-1}$ (use Equations (26) and (27)). Hence, spiral galaxies of fixed β satisfy

$$j \propto M \tag{28}$$

with a proportionality factor that decreases monotonically with increasing β.

In brief, late-type galaxies scatter around a mean relation $j \propto M^{2/3}$, representing 3D self-similarity (fixed volume density profile), while any subsample of fixed β follows a relation $j \propto M$, representing 2D self-similarity (fixed surface density profile). Together, these scalings naturally explain why the bulge fraction of spiral galaxies tends to increase with their mass (see Figure 9 gray shading versus solid lines).

6. CONCLUSIONS

This paper presented the first precision measurements (a few percent statistical uncertainty) of the specific angular momentum j in stars and baryons (stars, atomic gas, and molecular gas) in nearby spiral galaxies. The study relies on all 16 spiral (Sab-Scd) galaxies of the THINGS sample with stellar and cold gas surface densities published by Leroy et al. (2008). They cover baryon masses M_b of 10^9–$10^{11}\,M_\odot$ and bulge mass fractions β (=B/T) up to 0.32, representative of most galaxies in the local universe (Weinzirl et al. 2009). The relations between M (for baryonic M_b or stellar M_*), j (for j_b or j_*), and morphology were determined with unprecedented accuracy. The key findings are as follows.

1. M, j, and β are strongly and irreducibly correlated. Their mean relation given in Equations (9) and (10) and visualized in Figure 6 is consistent with no intrinsic scatter.
2. For a fixed β, the residual scaling is $j \propto M^\alpha$ with $\alpha \approx 1$, thus β varies monotonically with jM^{-1}. The exponent $\alpha \approx 1$ is larger than those found by Romanowsky & Fall (2012) for late-type galaxies of a fixed Hubble type. It is also larger than the exponent $\alpha \approx 2/3$ obtained for all late-type galaxies, without fixing β. This explains why β tends to increase with the mass of spiral galaxies (see Figure 9 gray shading versus solid lines).
3. The relations M_b–j_b–β and M_*–j_*–β are very similar with fitting parameters consistent within their uncertainties. This similarity is partially coincidental and holds despite the fact that cold gas contributes significantly (30%–40%) to the baryon angular momentum J_b with a specific angular momentum about twice that of stars.
4. The M–j–β relation persists, when considering only the contribution to M and j from the disk without the bulge: the disk "knows" about the bulge via its angular momentum. Therefore, it is impossible to explain the M–j–β relation of spiral galaxies from independent M–j relations of the disk and bulge.
5. The FP of spiral galaxies arises when the (M, j) plane is mapped into 3D (L, R, V) space via Equations (20). Therefore the FP and its projections, such as the TF relation, can be explained from the M–j relation.

Koda et al. (2000) wrote "We hypothesize that the 2D distribution [in the FP] implies the existence of two dominant physical factors in spiral galaxy formation... ." This work suggests that mass and angular momentum are the two fundamental factors. With hindsight, the tight relation between M, j, and morphology, and similar relations for early-type galaxies (Cappellari et al. 2011), justifies the historical classification of galaxies by stellar mass and Hubble type. As IFS-based measurements of j become easier, this historical classification might be substituted for a more fundamental and physically motivated classification by M and j.

D.O. thanks Aaron Romanowsky, Camille Bonvin, and Martin Bruderer for their helpful advice. We are grateful to the THINGS, SINGS, *GALEX*, HERACLES, and BIMA SONG teams for making their data publicly available. This research has made use of the NASA/IPAC Extragalactic Database (NED), which is operated by the Jet Propulsion Laboratory, California Institute of Technology, under contract with the National Aeronautics and Space Administration (NASA).

APPENDIX A
DECOMPOSITION IN DISK AND BULGE

For each of the 16 galaxies, the stellar mass fraction β of the "bulge" is calculated by fitting $\Sigma_*(r)$ with a model composed of an exponential function for the disk (d) and a Sérsic profile (Sérsic 1963) for the bulge (b),

$$\Sigma_\mathrm{fit}(r) = \underbrace{k_\mathrm{d} \exp\left[-\frac{r}{R}\right]}_{\Sigma_\mathrm{d}(r)} + \underbrace{k_\mathrm{b} \exp\left[-\left(\frac{r}{r_\mathrm{b}}\right)^{1/n}\right]}_{\Sigma_\mathrm{b}(r)}, \tag{A1}$$

where $k_\mathrm{d}, R, k_\mathrm{b}, r_\mathrm{b}$, and $n > 1$ (the "Sérsic index") are free parameters. Those are fitted to $\lg \Sigma_*(r)$ using a robust fitting method (Street et al. 1988) on the interval $r \in [0, \min(5R_*, R_\mathrm{max})]$, where R_* is the disk scale radius determined by Leroy et al. (2008) and given in Table 1, and R_max is the maximal radius to

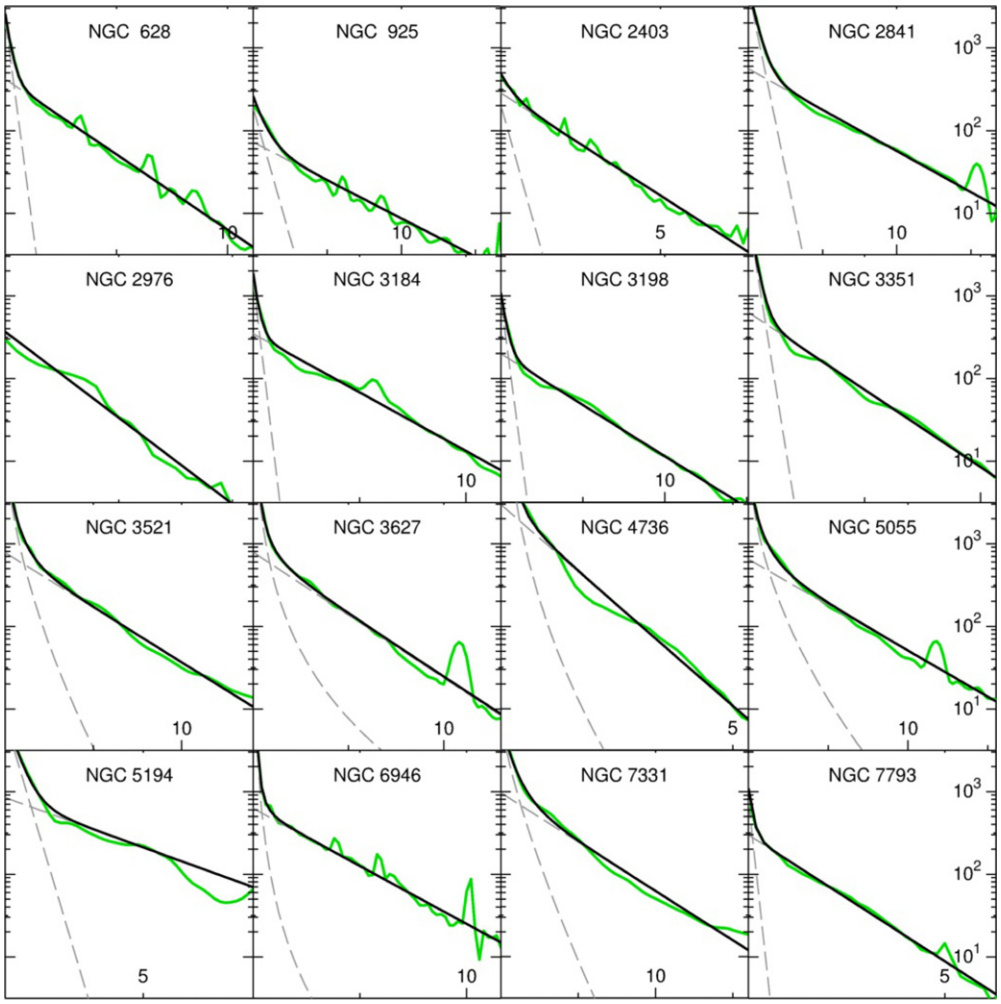

Figure 14. Decompositions of the stellar surface density profiles $\Sigma_*(r)$ into disks and bulges. Green solid lines show the measured $\Sigma_*(r)$, black solid lines show the fits $\Sigma_{\rm fit}(r)$ of Equation (A1), and gray dashed lines represent the two components $\Sigma_{\rm d}(r)$ and $\Sigma_{\rm b}(r)$.
(A color version of this figure is available in the online journal.)

which measurements for $\Sigma_*(r)$ were published by Leroy et al. The fits $\Sigma_{\rm fit}(r)$ and their components $\Sigma_{\rm d}(r)$ and $\Sigma_{\rm b}(r)$ are plotted in Figure 14. Given those fits, the bulge mass fractions become $\beta = \int drr\Sigma_{\rm b}(r)/\int drr\Sigma_{\rm fit}(r)$. The standard errors of β are typically around 0.02 as determined from multiple resampling of the data (Efron & Tibshirani 1993).

APPENDIX B

ANGULAR MOMENTUM MEASUREMENT

Let us consider a flat galaxy with circular orbits, tilted against the observer by the inclination angle i, as shown in Figure 15. Here, this inclination i is assumed to be known, since adopted from Leroy et al. (2008), but otherwise it can be determined from fits to the kinematic maps or from the minor-to-major axis ratio of the galaxy (e.g., Obreschkow et al. 2013). Any orbiting point P of mass dM has a position vector $\mathbf{r}$ and a velocity vector $\mathbf{v} \perp \mathbf{r}$. The scalar angular momentum of the disk is given by

$$J = \left| \int dM \mathbf{r} \times \mathbf{v} \right| = \int dMrv$$
$$= \int_0^\infty drr^2 \int_0^{2\pi} d\theta \Sigma(r,\theta) v(r,\theta), \qquad \text{(B1)}$$

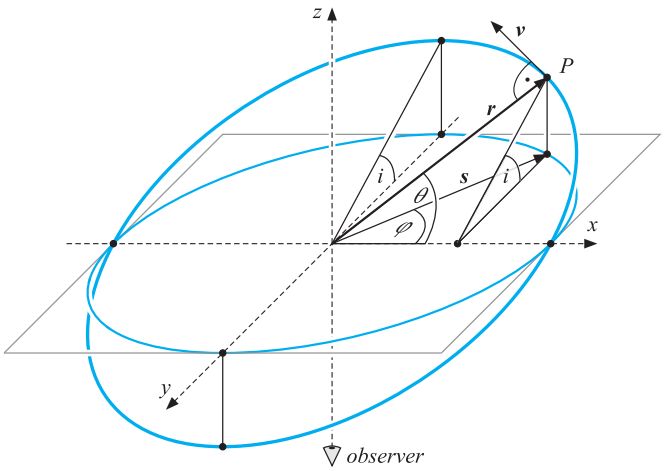

Figure 15. Schematic visualization of a particle P on a circular orbit inclined against the line-of-sight.
(A color version of this figure is available in the online journal.)

where Σ denotes the mass surface density of a specific baryonic component (e.g., stars). Upon assuming that the orbital velocity v does not depend on θ, or at least that variations of v with θ are uncorrelated to the variations of Σ with θ—an assumption found

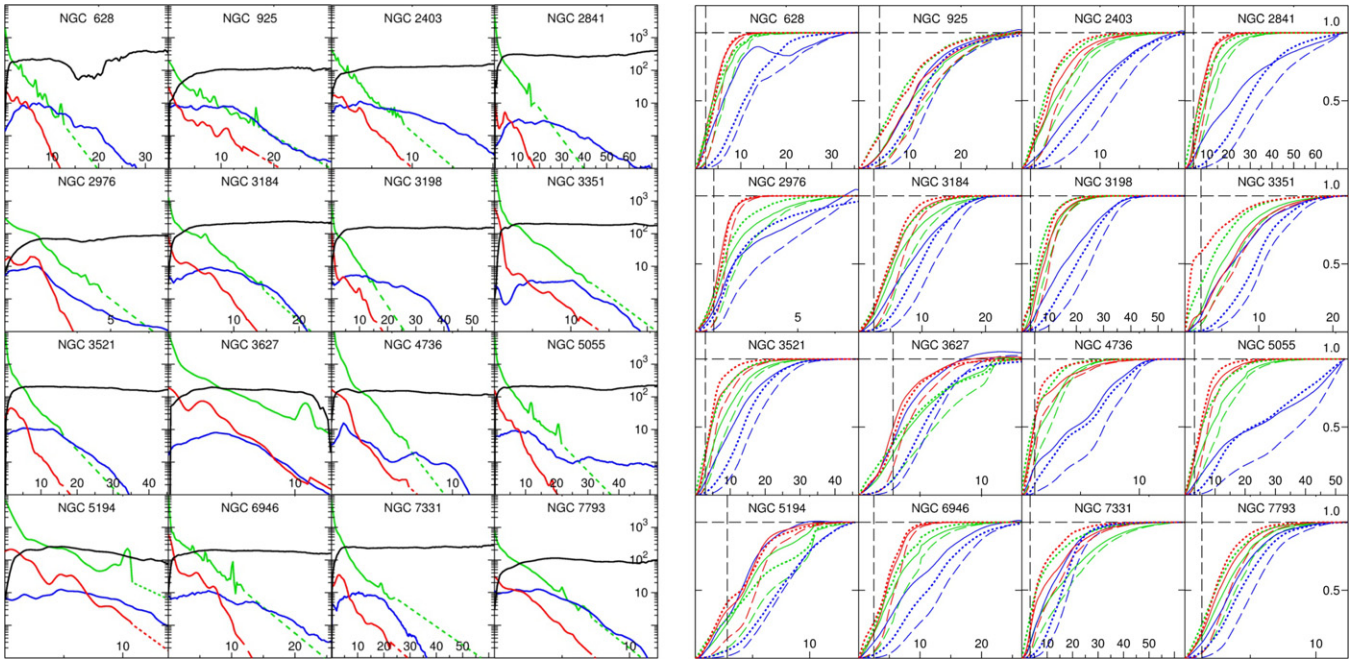

Figure 16. Left: inclination-corrected, azimuthally averaged circular velocity profiles $v(r)$ in units of km s^{-1} (black), extracted from the H I velocity maps; and inclination-corrected, azimuthally averaged mass surface densities of stars (green), H I (blue), and H_2 (red) in units of $M_\odot$ pc^{-2}. Solid colored lines represent the measurements adopted from Leroy et al. (2008) for stars and H_2 and extracted from the H I intensity maps of Walter et al. (2008) for H I. Dashed lines represent exponential extrapolations, where no data is available. Right: normalized cumulative functions of mass $M(r)$ (dotted, Equation (B6)), angular momentum $J(r)$ (dashed, Equation (B7)), and specific angular momentum $j(r)$ (solid, Equation (B8)). Different colors represent stars (green), H I (blue), and H_2 (red).

(A color version of this figure is available in the online journal.)

correct at the 1% level—the second integral can be separated to $2\pi\Sigma(r)v(r)$ with $\Sigma(r) \equiv (2\pi)^{-1}\int_0^{2\pi} d\theta\Sigma(r,\theta)$ and $v(r)$ being some azimuthally averaged mean of $v(r,\theta)$. Thus,

$$J = 2\pi\int_0^\infty dr r^2\Sigma(r)v(r). \tag{B2}$$

Note that this simplification to radial profiles only does *not* require or assume $\Sigma(r,\theta)$ to be invariant of θ. To evaluate J via Equation (B2), $v(r)$ is needed, which requires measurements of r and v across the galaxy. However, these variables are not directly observable. Instead, for any pixel in the H I maps (Figure 2, left), one measures the projected radius s, its projected azimuth φ (i.e., the angle between the major axis and **s**) and the recession velocity v_z. It is therefore necessary to calculate r and v from s, φ, v_z and i. These relations are easily derived from Figure 15 using basic trigonometry. Evoking the Pythagorean theorem,

$$r = \left(r_x^2 + r_y^2 + r_z^2\right)^{1/2} = \left[(s\cos\varphi)^2 + (s\sin\varphi)^2 + (s\sin\varphi\tan i)^2\right]^{1/2} = s(\cos^2\varphi + \sin^2\varphi\cos^{-2} i)^{1/2}. \tag{B3}$$

If $i = 90^\circ$, the galaxy aligns with the (x, z)-plane and similarity implies $r_x/r = v_z/v$. As i decreases, r_x, r and v remain unchanged, while v_z must be substituted for $v_z\sin^{-1} i$, thus $r_x/r = v_z/(v\sin i)$. Using Equation (B3), v then solves to

$$v = \frac{r}{r_x}\frac{v_z}{\sin i} = \frac{(\cos^2\varphi + \sin^2\varphi\cos^{-2} i)^{1/2}}{\cos\varphi\sin i}v_z \equiv C(\varphi, i)\, v_z, \tag{B4}$$

where we introduced the local velocity deprojection factor $C(\varphi, i)$. Note that the term r/r_x cannot be simplified to $(1 + \tan^2\varphi\cos^{-2} i)^{1/2}$, since $(\cos^2\varphi)^{1/2} \neq \cos\varphi$ if $\cos\varphi < 0$.

To evaluate the function $v(r)$ of a real galaxy, Equations (B3) and (B4) are applied to every pixel k in the 2D H I map (2048 × 2048 pixels for NGC 2403, 1024 × 1024 pixels for the other 15 galaxies). Using both the intensity (moment 0) and velocity (moment 1) maps, each pixel k is given a value $\{I_k, r_k, v_k\}$, where I_k denotes the intensity. The data is then binned into different radii, equally spaced by 100 pc. In every bin, the mean velocity is calculated as the mean of the pixel velocities, weighted by intensity and the variance $C(\varphi, i)^{-2}$ of the deprojection error,

$$v_{\rm bin} = \frac{\sum_{k\in{\rm bin}} I_k C(\varphi, i)^{-2} v_k}{\sum_{k\in{\rm bin}} I_k C(\varphi, i)^{-2}}. \tag{B5}$$

This results in a discrete function $v(r)$ known at steps of 100 pc. In turn, the different density profiles $\Sigma(r)$ are given at 200 pc to 700 pc spacings. These profiles are re-gridded to 100 pc spacings using a spline-interpolation in order to multiply them with $v(r)$ in the computation of J.

Figure 16 (left) shows the radial surface densities $\Sigma(r)$ of stars, H I, and H_2 (including helium) together with the extracted velocity profiles $v(r)$. The corresponding normalized cumulative functions of mass and angular momentum are shown in Figure 16 (right). They are defined as

$$M(r) = 2\pi\int_0^r dr' r'\Sigma(r'), \tag{B6}$$

$$J(r) = 2\pi\int_0^r dr' r'^2\Sigma(r')v(r'), \tag{B7}$$

$$j(r) = J(r)/M(r). \tag{B8}$$

Models of $M(r)$, $J(r)$, and $j(r)$ based on an exponential disk (see Equation (3) for $j(r)$) are used to estimate the uncertainty of M, J, and j due to the finite size of the maximal observable radius $R_{\rm max}$. In the limit of this exponential model, the relative difference between $j(R_{\rm max})$ and j is 45.6%, 8.7%, and 0.2%, if $R_{\rm max}/R = 2, 5$, and 10, respectively, where R is the exponential scale radius of $\Sigma(r)$. Since most galaxies studied here were measured to $R_{\rm max} \approx 10R$ for stars and H_2 (with extrapolations to the H I radii $R_{\rm max,HI} \approx 14R$), the values j_* and j_{H_2} are converged to less than 1%. Explicit fits of Equation (3) to the measured $j(r)$ suggest that $j_{\rm b}$, j_*, and j_{H_2} are converged at the 1% level, while $j_{\rm gas}$ and $j_{\rm HI}$ are converged at the 10% level. Only in the case of NGC 5055 $j_{\rm HI}$ might be 30% larger than measured, but even in this case the baryonic $j_{\rm b}$ changes by less than 10%. Additional statistical and systematic uncertainties are discussed in Section 2.3. As a sanity check of the deprojection method, the Pearson correlation coefficient c between the inclinations i and the values $j_{\rm b}$ was computed and revealed no significant correlation ($c \approx 0.2$).

APPENDIX C

MULTIVARIATE LINEAR REGRESSIONS

The bivariate linear regression is a method to fit the linear equation

$$y = k_1 x + k_2 \tag{C1}$$

with free parameters k_1 and k_2 to a set of 2D data points. This regression is optimal in the sense that it provides the most likely linear relation for data that intrinsically lies on a linear relation, but has been scattered by uncorrelated Gaussian noise of known variance. This noise can apply to both dimensions and may be different for each data point. The bivariate linear regression is obtained by minimizing

$$\chi^2 = \sum_i \frac{(k_1 x_i + k_2 - y_i)^2}{k_1^2 \sigma_{x,i}^2 + \sigma_{y,i}^2}, \tag{C2}$$

where (x_i, y_i) are the measured values and $\sigma_{x,i}^2$ and $\sigma_{y,i}^2$ are their variances in both dimensions.

In the same sense, the trivariate linear regression is the optimal method to fit the linear equation

$$z = k_1 x + k_2 y + k_3 \tag{C3}$$

with free parameters k_1, k_2, and k_3 to a set of 3D data points. This regression is obtained by minimizing

$$\chi^2 = \sum_i \frac{(k_1 x_i + k_2 y_i + k_3 - z_i)^2}{k_1^2 \sigma_{x,i}^2 + k_2^2 \sigma_{y,i}^2 + \sigma_{z,i}^2}, \tag{C4}$$

where (x_i, y_i, z_i) are the measured values and $\sigma_{x,i}^2$, $\sigma_{y,i}^2$, and $\sigma_{z,i}^2$ their variances.

In this work, the χ^2 minimization is performed using MATLAB's "fminsearch" function, which relies on the Nelder-Mead simplex algorithm as described by Lagarias et al. (1998).

REFERENCES

Agertz, O., Teyssier, R., & Moore, B. 2011, MNRAS, 410, 1391
Arimoto, N., Sofue, Y., & Tsujimoto, T. 1996, PASJ, 48, 275
Arnold, J. A., et al. 2013, arXiv:1310.2607
Barnes, D. G., Staveley-Smith, L., de Blok, W. J. G., et al. 2001, MNRAS, 322, 486
Beauvais, C., & Bothun, G. 1999, ApJS, 125, 99
Behroozi, P. S., Wechsler, R. H., & Conroy, C. 2013, ApJ, 770, 57
Benson, A. J. 2012, NewA, 17, 175
Blitz, L., & Rosolowsky, E. 2006, ApJ, 650, 933
Boissier, S., Prantzos, N., Boselli, A., & Gavazzi, G. 2003, MNRAS, 346, 1215
Bournaud, F., Perret, V., Renaud, F., et al. 2014, ApJ, 780, 57
Brooks, A. M., Solomon, A. R., Governato, F., et al. 2011, ApJ, 728, 51
Cappellari, M., Emsellem, E., Krajnović, D., et al. 2011, MNRAS, 413, 813
Cervantes-Sodi, B., Li, C., Park, C., & Wang, L. 2013, ApJ, 775, 19
Ceverino, D., Dekel, A., Mandelker, N., et al. 2012, MNRAS, 420, 3490
Cole, S., & Lacey, C. 1996, MNRAS, 281, 716
Courteau, S., Dutton, A. A., van den Bosch, F. C., et al. 2007, ApJ, 671, 203
Croom, S. M., Lawrence, J. S., Bland-Hawthorn, J., et al. 2012, MNRAS, 421, 872
de Blok, W. J. G., Walter, F., Brinks, E., et al. 2008, AJ, 136, 2648
Dorman, C. E., Guhathakurta, P., Fardal, M. A., et al. 2012, ApJ, 752, 147
Doroshkevich, A. G. 1970, Afz, 6, 581
Efron, B., & Tibshirani, R. 1993, An Introduction to the Bootstrap, Monographs on Statistics and Applied Probabilities (Boca Raton: CRC)
Elmegreen, B. G., Bournaud, F., & Elmegreen, D. M. 2008, ApJ, 688, 67
Fall, S. M. 1983, in IAU Symp. 100, Internal Kinematics and Dynamics of Galaxies, ed. E. Athanassoula (Cambridge: Cambridge Univ. Press), 391
Fall, S. M., & Romanowsky, A. J. 2013, ApJL, 769, L26
Flynn, C., Holmberg, J., Portinari, L., Fuchs, B., & Jahreiß, H. 2006, MNRAS, 372, 1149
Genel, S., Naab, T., Genzel, R., et al. 2012, ApJ, 745, 11
Genzel, R., Newman, S., Jones, T., et al. 2011, ApJ, 733, 101
Gil de Paz, A., Boissier, S., Madore, B. F., et al. 2007, ApJS, 173, 185
Glazebrook, K. 2013, PASA, 30, e056
Governato, F., Brook, C., Mayer, L., et al. 2010, Natur, 463, 203
Guedes, J., Callegari, S., Madau, P., & Mayer, L. 2011, ApJ, 742, 76
Guo, Y., Giavalisco, M., Ferguson, H. C., Cassata, P., & Koekemoer, A. M. 2012, ApJ, 757, 120
Han, J., Deng, Z., Zou, Z., Wu, X.-B., & Jing, Y. 2001, PASJ, 53, 853
Helfer, T. T., Thornley, M. D., Regan, M. W., et al. 2003, ApJS, 145, 259
Hernandez, X., & Cervantes-Sodi, B. 2006, MNRAS, 368, 351
Kalberla, P. M. W., & Dedes, L. 2008, A&A, 487, 951
Kannappan, S. J., Fabricant, D. G., & Franx, M. 2002, AJ, 123, 2358
Kennicutt, R. C. J., Armus, L., Bendo, G., et al. 2003, PASP, 115, 928
Kent, S. M. 1986, AJ, 91, 1301
Kent, S. M. 1987, AJ, 93, 816
Kent, S. M. 1988, AJ, 96, 514
Knebe, A., & Power, C. 2008, ApJ, 678, 621
Koda, J., Milosavljević, M., & Shapiro, P. R. 2009, ApJ, 696, 254
Koda, J., Sofue, Y., & Wada, K. 2000, ApJL, 531, L17
Komatsu, E., Smith, K. M., Dunkley, J., et al. 2011, ApJS, 192, 18
Kormendy, J., & Fisher, D. B. 2008, in ASP Conf. Ser. 396, Formation and Evolution of Galaxy Disks, ed. J. G. Funes & E. M. Corsini (San Francisco, CA: ASP), 297
Lagarias, J. C., Reeds, J. A., Wright, M. H., & Wright, P. E. 1998, SIAM Journal of Optimization, 9, 112
Lawrence, J., Bland-Hawthorn, J., Bryant, J., et al. 2012, Proc. SPIE, 8446, 844653
Leroy, A. K., Walter, F., Bigiel, F., et al. 2009, AJ, 137, 4670
Leroy, A. K., Walter, F., Brinks, E., et al. 2008, AJ, 136, 2782
Macciò, A. V., Dutton, A. A., & van den Bosch, F. C. 2008, MNRAS, 391, 1940
Marinacci, F., Pakmor, R., & Springel, V. 2013, MNRAS, 437, 1750
McGaugh, S. S., Schombert, J. M., de Blok, W. J. G., & Zagursky, M. J. 2010, ApJL, 708, L14
McMillan, P. J. 2011, MNRAS, 414, 2446
Meyer, M. J., Zwaan, M. A., Webster, R. L., Schneider, S., & Staveley-Smith, L. 2008, MNRAS, 391, 1712
Mo, H. J., Mao, S., & White, S. D. M. 1998, MNRAS, 295, 319
Navarro, J. F., & Steinmetz, M. 2000, ApJ, 538, 477
Obreschkow, D., Heywood, I., & Rawlings, S. 2011, ApJ, 743, 84
Obreschkow, D., Ma, X., Meyer, M., et al. 2013, ApJ, 766, 137
Obreschkow, D., & Rawlings, S. 2009a, MNRAS, 400, 665
Obreschkow, D., & Rawlings, S. 2009b, ApJL, 696, L129
Obreschkow, D., & Rawlings, S. 2009c, MNRAS, 394, 1857
Paturel, G., Petit, C., Prugniel, P., et al. 2003, A&A, 412, 45
Peebles, P. J. E. 1969, ApJ, 155, 393
Prieto, M., Campos-Aguilar, A., & Garcia, C. 1989, Ap&SS, 157, 321
Read, J. I., & Trentham, N. 2005, RSPTA, 363, 2693
Romanowsky, A. J., & Fall, S. M. 2012, ApJS, 203, 17
Sánchez, S. F., Kennicutt, R. C., Gil de Paz, A., et al. 2012, A&A, 538, A8
Sandage, A., Freeman, K. C., & Stokes, N. R. 1970, ApJ, 160, 831
Sanders, D. B., Solomon, P. M., & Scoville, N. Z. 1984, ApJ, 276, 182

Sérsic, J. L. 1963, BAAA, 6, 41
Shen, S., Mo, H. J., & Shu, C. 2002, MNRAS, 331, 259
Steinmetz, M., & Bartelmann, M. 1995, MNRAS, 272, 570
Stewart, K. R., Brooks, A. M., Bullock, J. S., et al. 2013, ApJ, 769, 74
Stinson, G. S., Bailin, J., Couchman, H., et al. 2010, MNRAS, 408, 812
Street, J. O., Carroll, R. J., & Ruppert, D. 1988, The American Statistician, 42, 152
Toomre, A. 1964, ApJ, 139, 1217
Unwin, S. C. 1983, MNRAS, 205, 787
Walter, F., Brinks, E., de Blok, W. J. G., et al. 2008, AJ, 136, 2563
Walter, F., Weiss, A., Martin, C., & Scoville, N. 2002, AJ, 123, 225
Weinzirl, T., Jogee, S., Khochfar, S., Burkert, A., & Kormendy, J. 2009, ApJ, 696, 411
White, S. D. M. 1984, ApJ, 286, 38
Wuyts, S., Förster Schreiber, N. M., Genzel, R., et al. 2012, ApJ, 753, 114
Yegorova, I. A., & Salucci, P. 2007, MNRAS, 377, 507